A Mission to Image the Solar Gravitational Lens

AE460 Final Report

Wyatt Welch, Jayden Thomas, Arian Mazdeh, Nicklous Ngo, Luis Salas, Ethan Dueck, Bilal Kaou, Parham Khodadi, Leopoldo Gutierrez

San Diego State University, Department of Aerospace Engineering

This paper discusses the design parameters for a deep-space mission developed for Team Destiny's senior design project at San Diego State University (SDSU). The purpose of this mission is to capture light from the Einstein Ring formed from target planets around our Sun, harnessing a Solar Gravitational Lens (SGL). The images created from the processing of the Einstein Ring will allow us to analyze the target planet's surface at a resolution that will reveal information about the atmosphere, geography, and signs of habitability. The primary payload makes use of Einstein's theory of General Relativity by using the Sun's gravity to harness the bending and focusing of light from planets up to 100 light-years away. By maneuvering within the focal region, a spacecraft can observe planets and other bodies from a range of (650-900) au away from the sun with extreme resolution. The background of the project will be reviewed, followed by the mission objective, mission schedule, risk and budget. This report will then go over all major technical design parameters and verifications for our Payload, Data Handling, Electrical, Telemetry, Tracking and Control, Flight Dynamics, Attitude Dynamics, Mechanical, and Thermal subsystems for this mission. Major design analyses have been performed and finalized regarding each subsystem, including simulations. Each subsystem will have a simulated verification, in addition, we provide a Model of the spacecraft, and a full GUI for synthetic telemetry and events. Finally, we provide hardware to capture the image of a planet, process it into an Einstein ring, then deconvolute it into a 2D image using only data from the ring.

Contents

I. Introduction

A. Background

The Solar Gravitational Lens (SGL) harnesses the principle of gravitational lensing and Einstein's theory of General Relativity by using the solar gravitational field's diffraction of electromagnetic waves that travel within proximity of the sun. This effect turns the sun into a very large aperture lens. The focus of light around the sun forms an *Einstein Ring*, a circular ring of light around the sun, showing the magnified image of distant exoplanets. Though 550 au is where this effect begins, the effective focal range for a spacecraft begins at 650 au, providing more usable light collection. Putting a spacecraft in that region, the rings light can be collected, processed, deconvoluted, then downlinked as a 2D image of the target object.

The main scientific motivation for this mission is the direct imaging of exoplanets. Proxima Centauri b (PCb) will be the main selection, captured at a kilometer-scale spatial resolution. This level of detail enables analysis of surface features including oceans, atmospheric composition, climate, and a potential for biosignatures. Proxima Centauri B is chosen because it is the closest planet in a Goldilocks zone, with the highest potential for outer-system pioneering due to many other exoplanets existing close to it. The close distance also minimizes the effect of stellar wobble — the effect of PCb's solar system circling at a different rate to our sun, requiring the spacecraft to continuously spiral to keep the sun between the spacecraft and the target planet [1]. This type of imaging was only thought to be theoretical in the past, as the current technology on telescopes are very limited. This is primarily due to the difficulty of reaching the focal region in an acceptable time frame. Harnessing the sun as a massive aperture lens, it is the only current feasible option for high detailed imaging of non self-luminous planets far outside of our solar system.

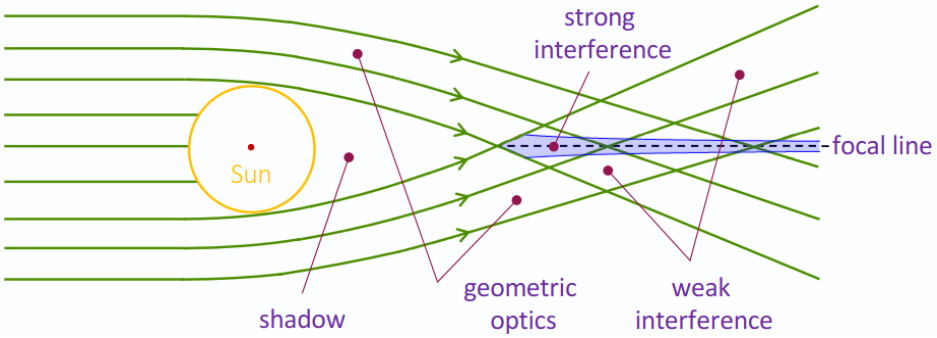

Fig. 1 Different Optical Regions of the SGL (Adapted from [2])

B. Mission Objectives

The primary mission objective is to utilize the Solar Gravitational Lens to reconstruct PCb from the mid-IR light amplified and focused by the Sun's gravitational field. We convert the Einstein ring brightness measurements into planetary image data using onboard processing and later ground based image refinement after downlink, This is because we cannot use the detector as a direct photograph output due to the long image integration times required. The image resolution target is on the order of 1 megapixel, however due to increased noise over long deconvolution times, 256x256 and 512x512 pixel images would likely produce higher quality images. The initial image should take an estimated 1.6 years of cumulative data collection. With PCb being located 4.24 ly away, the image quality should produce an estimated 43x43 km output per pixel of the planets surface (in the event of a 1024x1024 image). Further objectives require maintaining angular measurement and pointing on the order of 0.01 arc-seconds in order to keep the spacecraft aligned with the SGL optical axis and receive TT&C uplink from Earth. We must also demonstrate a high-energy outbound mission including a Jupiter gravity assist, a solar Oberth, and solar-sail deployment in order to reach the SGL focal region in the shortest time possible. The demonstration of solar-sail technology as a primary propulsion method for rapid solar-system escape is another objective, as it is highly untested in practice. We must also survive extreme thermal environments from the sun dive, as well as as extreme colds and radiation during the deep-space cruise, where the only natural heat is that of the Cosmic Background Radiation.

C. System Overview

The spacecraft operates as a single autonomous SGL telescope that cruises to the target line of sight opposite PCb, keeping the sun between the planet and the spacecraft. The mission begins with Earth departure, followed by a Jupiter gravity assist, a solar Perihelion/Oberth, solar sail deployment directly after, and a long hyperbolic cruise out to the SGL focal region after detaching the solar sail at 30 au. Once the spacecraft reaches 650 au, the science phase begins and we image the ring until reaching the end of the focal region at 900 au. The payload uses a meter-class telescope, internal Lyot Coronagraph, Polarimetric filtering, and hyperspectral image collection to gather the faint Einstein Ring light while suppressing the solar disk and coronal light. The collected light is digitized and processed in the On Board Computer (OBC), for future image reconstruction. The ADCS maintains fine pointing towards the Sun / ring geometry during the science phase. The OBC acts as the central command and data hub, collecting telemetry, scheduling tasks, storing science data, performing image reconstruction, and managing fault detection autonomously (due to the multi-day communication delay for deep space travel).

D. Schedule

The SGL mission requires careful scheduling and planning, due to a window of opportunity that repeats once every 11.86 Earth years (the orbital period of Jupiter). Combining this opportunistic approach with the mission's long-term nature, our schedule spans the entirety of the rest of this century. After the necessary preparations, the mission will launch in 2049, conduct gravity assist maneuvers in the solar system until 2058, and finally reach 650 au in the direction of anti-Proxima Centauri b (α = 02 : 29 : 42.944853 HMS; δ = 62 : 40 : 46.1631 DMS) by 2096.

2025-2026	Initial Mission Design
2026-2028	Mission Design Finalization
2028-2030	Initial Funding and Contracting
2030-2049	Manufacturing and Testing
2049	Launch and Earth Escape
2054	Jupiter Flyby
2056	Solar Sail Deployment and Solar Flyby
2058	Pass 30 au from the Sun and Detach Sail
2058-2096	Cruise to 650 au in the direction of anti-Proxima Centauri b
2096	Reach 650 au, begin spiraling motion, and begin imaging
2124+	900 au reached, final downlink and decommission

Table 1 Mission Schedule

E. Risk Management

Risk management is a very important component of the Solar Gravitational Lens (SGL) mission design due to the extreme operational environment we are dealing with, as well as the length of the mission duration and our limited opportunity for real-time intervention. The spacecraft must operate autonomously for decades while enduring high thermal loads near perihelion, deep-space cold conditions, radiation exposure, and stringent pointing requirements. In order to address these challenges, we have put together a structured risk assessment in an attempt to identify the highest-impact risks across all of our mission phases. This includes Launch and Early Operations (LEOP), Jupiter and solar Oberth maneuvers, long-duration cruise, and science operations. We have identified each of these risks in terms of their likelihood and consequences. Mitigation strategies have also been defined along with subsystem ownership.

Table 2 Mission Risk Assessment and Mitigation Strategy

Risk	Likelihood	Consequence	Mitigation Strategy	Owner
ADCS failure (loss of pointing)	Medium	Critical	Use of redundant sensors (star trackers, gyros), reaction wheel monitoring, autonomous FDIR, and safe-mode stabilization routines	ADCS
Solar sail deployment failure	Low	Critical	Extensive ground testing, deployment monitoring, and conservative deployment sequencing prior to perihelion	Mechanical / Propulsion
Telescope deployment failure	Low	Critical	Redundant deployment mechanisms, pre-science verification, and protective stowage during cruise	Payload / Mechanical
Encoder/decoder failure (loss of communication)	Low	Critical	Redundant communication pathways, radiation-hardened electronics, and error correction protocols	COM / OBDH
Optical communication link degradation (pointing error, weather, noise)	Medium	High	Multiple ground stations, adaptive coding/modulation, high-precision pointing control, and link margin design	COM / ADCS
Thermal overload during perihelion	Low	Critical	Carbon–carbon heat shield, reflective coatings, precise spacecraft pointing, and radiator sizing	Thermal
Insufficient heating in deep space	Medium	High	Use of MLI insulation, RTG waste heat, radioisotope heater units (RHUs), and trim heaters	Thermal / EPS
Radiation-induced electronics failure	High	High	Radiation-hardened components, shielding, error detection and correction (EDAC), and cold-redundant architecture	OBDH / EPS
End-of-life power degradation (RTG decay)	Medium	High	Conservative power budgeting, load prioritization, battery buffering, and reduced duty cycles for high-power operations	EPS

The overall mitigation strategy for the SGL mission is based on a combination of redundancy, autonomy, and conservative design margins. Many of our critical subsystems attempt to incorporate cold-redundant architectures to try to reduce single-point failures while also minimizing continuous power consumption. The process of Autonomous Fault Detection, Isolation, and Recovery (FDIR) enables the spacecraft to respond to anomalies without any sort of ground intervention. This is essential for our mission because of the multi-day communication delays involved. The thermal and power subsystems are designed with conservative margins to ensure the survivability of the spacecraft in both extreme hot and cold environments. The operational procedures will enforce constraints on high-power activities, such as downlink communications, to prevent exceeding our thermal or energy limits of the mission. The operations of our mission will also rely on pre-validated command sequences and on the support of distributed ground stations on Earth to maintain the robustness of our mission over several decades. Overall, these key strategies that we implement will ensure that our mission risks will be significantly reduced to acceptable levels while also maintaining the feasibility and reliability of our long-term deep-space operations.

II. Systems Engineering

A. Requirements and Verification Overview

Table 3 Requirements Verification Matrix

Req ID	Requirement	Method	Evidence
MR-1	Exoplanet imaging using Solar Gravitational Lens	Test	Mission objective; Payload Subsystem; Status: Met
MR-2	Operate between 650–900 au	Analysis	Parent: MR-1; Optimal SGL range; Subsystem: All; Status: Met
MR-3	Reach 650 au within 47 years	Analysis	Parent: MR-1; Lifetime feasibility; Subsystem: FDS, Propulsions; Status: Met
MR-4	Achieve $\geq$20 au/year exit velocity via solar sail	Analysis	Parent: MR-3; Enables timeline; Subsystem: Propulsion; Status: Met
MR-5	Spacecraft bus mass $\leq$ 150 kg	Inspection	Parent: MR-3; Solar sail feasibility; Subsystem: All; Status: Met
MR-6	Delivered to orbit before solar transfer	Inspection	Parent: MR-1; Launch prep; Subsystem: FDS; Status: Met
MR-7	Fit within launch vehicle volume	Inspection	Launch provider constraint; Subsystem: FDS; Status: Met
MR-8	Identify Earth-like target within $\sim$100 ly	Analysis	Parent: MR-1; Imaging feasibility; Subsystem: Payload; Status: Met
MR-9	Maintain science operations for 10 years post-arrival	Analysis	Parent: MR-1; Imaging duration; Subsystem: Payload; Status: Met
MR-10	Survive deep-space environment for 40+ years	Test	Parent: MR-9; Radiation/thermal reliability; Subsystem: All; Status: Met
MR-11	Attitude $\leq$1 m, velocity $\leq$1 cm/s accuracy	Test	Parent: MR-10; Navigation precision; Subsystem: CDH; Status: Met
MR-12	Telescope aperture $\geq$ 1 m	Demonstration	Parent: MR-1; Imaging resolution; Subsystem: Payload; Status: Met
MR-13	Solar suppression $\leq 10^{-7}$ (coronagraph)	Demonstration	Parent: MR-1; Light contamination control; Subsystem: Payload; Status: Met
MR-14	Image-plane stability $\leq$ 1 m	Analysis	Parent: MR-12; Image quality; Subsystem: Payload; Status: Met
MR-15	Operate from -190°C to +700°C	Test	Parent: MR-10; Thermal extremes; Subsystem: Thermal; Status: Met
MR-16	Optical comms $\geq$100 bps to 900 au	Demonstration	Parent: MR-1; Data return; Subsystem: Communications; Status: Met
MR-17	Provide $\geq$100 W power over mission life	Test	Parent: MR-10; Power continuity; Subsystem: EPS; Status: Met
MR-18	Support modular in-flight assembly	Demonstration	Parent: MR-10; Scalable architecture; Subsystem: FDS; Status: Met
MR-19	Formation control accuracy $\leq$1 m	Test	Parent: MR-11; Multi-spacecraft imaging; Subsystem: CDH/GNC; Status: Met

B. Budget Updates

Tables 4-7 detail various budget updates for the mission, including the total mass, electrical power, mission cost and daily data budget. These graphs will visualize the parameters for which each system requires, further discussed in their respective subsections.

Table 4 Mass Budget Breakdown

System	Dimensions	Mass (kg)
Ejected Stage Structure	(1.5 m x 1.5 m x 3 m)	35
Final Stage Structure	(1.5 m x 1.5 m x 3 m)	35
Propellant (LOX + LCH4)	Tanks (varied volumes)	13284
Solar Sail	Deployed: 167772 m^2	167
Payload	Optical + instruments	22
Avionics (Sensors, OBC)	Varied	27
Low-Powered Thrusters	(80 mm x 80 mm)	8
Dry Mass (Final Stage)	–	37
Total Mass	–	**14714.1**

Table 5 Electrical Power Budget

Subsystem	Power (W)
TT&C	15
Payload	10
ADCS	28
Propulsion	15
Onboard CPU (Idle)	4
Onboard CPU (Max)	25
Thermal Heating	12

Table 6 Mission Cost Budget

Category	Cost (Million USD)
Concept / Design	300
Build / Development	401.3
Testing / Qualification	400
Launch	97
Operations	500
Total	**1698.3**

Table 7 Daily Data Budget

Data Source	Rate	Duty Cycle Volume/day (MB)	
Housekeeping Telemetry	2 kbps	50%	3.6
Payload Science Data	5 kbps	100%	18
Event Logs / FDIR	1 kbps	10%	0.36
Total	–	–	**21.96**

“‘latex

C. COTS Component Option Sheets

Table 8 Commercial Off-The-Shelf (COTS) Components and Payload Hardware Summary

Component	Vendor	Part #	Cost	Mass	Power	Lead Time	Radiation / Space Rating	Subsystem
Autonomous Star Tracker (4)	Sodern	SED 16-A	$100k–500k/unit	12 kg	40 W	12–18 mo	GEO/LEO rad tolerant	ADCS
Reaction Wheel Assembly (4)	Honeywell	HR04	$80k–250k/unit	10.5 kg	25 W	6–12 mo	>20 krad hardened	ADCS
1 m Primary Mirror	Custom	Custom	$15 M	8.5 kg	0 W	Full Flight	Deep-space qualified	Payload
Optical Bench	Custom	Custom	$2 M	1.4 kg	0.2 W	Full Flight	Deep-space qualified	Payload
Beam Splitters	Custom	Custom	$0.5 M	0.4 kg	0 W	Full Flight	Deep-space qualified	Payload
Internal Lyot Coronagraph	Custom	Custom	$6 M	1.4 kg	0.3 W	Payload Time	Deep-space qualified	Payload
Polarizer	Custom	Custom	$0.5 M	0.3 kg	0.1 W	Payload Time	Deep-space qualified	Payload
Hyperspectral Dispersion	Custom	Custom	$5 M	1.2 kg	0.8 W	Payload Time	Deep-space qualified	Payload
CCD Focal Plane + Electronics	Custom	Custom	$3 M	0.6 kg	1.2 W	Payload Time	Deep-space qualified	Payload
Detector Thermal Control	Minco	HK5578	$10k/unit	0.5 kg	0.7 W	Payload Time	Deep-space-qualified heater	Thermal
Payload Image Processor	Custom	Custom	$1.5 M	0.5 kg	0.7 W	Payload Time	Deep-space qualified	Payload
Payload Interface Electronics	Custom	Custom	$1.5 M	0.5 kg	0.7 W	Payload Time	Deep-space qualified	Payload
1 TB Science Storage	Custom	Custom	$0.5 M	0.2 kg	0.3 W	Payload Time	Deep-space qualified	Payload
Harnessing / Connectors	Custom	Custom	$1 M	0.9 kg	0.2 W	Payload Time	Deep-space qualified	Payload
Structural Frame	Custom	Custom	$5 M	70 kg	N/A	N/A	N/A	Mech.
Solar Shield	Custom	Custom	$5 M	20 kg	N/A	N/A	Thermal/rad shield	Mech.
Mechanical Arms	Custom	Custom	$1 M	5 kg	15 W	3 min deploy	N/A	Mech.
Misc. Hardware	Custom	Custom	$1.5 M	5 kg	5 W	Stage deploy	N/A	Mech.
MLI	Sheldahl	Custom	$0.5 M	5 kg	0 W	6–12 mo	Deep-space qualified	Thermal
Carbon-Carbon Heat Shield	CCAT	Custom	$5 M	20 kg	0 W	12–18 mo	Extreme thermal env.	Thermal
Trim Heaters	Kapton	HK5578	$10k/unit	0.5 kg	12 W	2–4 mo	Deep-space-qualified heater	Thermal
Radiator Panels	Northrop	Custom	$0.5 M	8 kg	0 W	8–12 mo	Deep-space-rated hardware	Thermal
BET-300-P Ionic Propulsion	Busek	Unknown	Quote Req.	0.166 kg	24 W	Payload Time	Not public	Prop.
Thrusters/Tanks	Custom	Custom	~ $2.5 M	1150 kg	~0 W	Full Flight	Thermal/rad tolerant	Prop.
Solar Sail	Custom	Custom	~ $3 M	167 kg	~0 W	Solar Oberth	Unknown	Prop.
Fuel (LOX/LCH_4/Hyd.)	Custom	Custom	~ $4k	12000 kg	0 W	Full Flight	Thermal/rad tolerant	Prop.
Optical Comm. Module	JPL	Custom	$20 M	3.6 kg	15 W	Full Flight	Full qualification	TT&C
NiH_2 Battery Cells	Custom	Custom	~ $1k/cell	1 kg	0 W	Full Flight	Full qualification	EPS
Lightweight Exploration RTG	Custom	Custom	$100k–500k/unit	200 g	0 W	Full Flight	Not public	EPS

D. AIV Overview

The Assembly, Integration and Verification (AIV) campaign for the SGL mission is designed to reduce risk for a spacecraft that requires over 40 years of autonomous survival in extreme thermal, radiation, and deep-space environments. The overall AIV integration involves a bottom-up verification approach, first looking at the component-level, moving up to subsystem and spacecraft integration. There will then be performance for environment analysis, demonstrations and testing following NASA practices.

Here is a summarized list of the primary integrations for the AIV flow:

1) **Component Qualification**
   - Radiation testing of avionics, processors, detectors, and communication electronics
   - Thermal vacuum cycling of payload optics and propulsion hardware
   - Functional verification of star trackers, reaction wheels, RTGs, and optical communication hardware
   - Solar sail material survivability testing under thermal and ultraviolet loading
2) **Subsystem Integration**
   - Payload optical bench assembly and alignment
   - ADCS integration with star trackers, gyros, and reaction wheels
   - Integration of propulsion stages and tank assemblies
   - TT&C optical terminal integration and alignment verification
   - Electrical power subsystem integration including RTGs, batteries, and power regulation hardware
3) **Spacecraft Bus Integration**
   - Structural frame integration
   - Harness routing and connector verification
   - Thermal hardware installation including MLI, radiators, trim heaters, and heat shield
   - Payload-to-OBC interface verification
   - Final mass properties measurements and center-of-gravity validation
4) **Stage Integration and Deployment Testing**

- Separation testing for jettisonable propulsion stages
- Solar sail deployment verification under simulated zero-gravity conditions
- Mechanical arm and deployment mechanism testing
- Optical alignment validation after deployment events

5) **System-Level Environmental Testing**
   - Random vibration testing for launch qualification
   - Acoustic testing for launch survivability
   - Shock testing for stage separation events
   - Thermal vacuum testing across expected mission temperature extremes
   - Electromagnetic interference/electromagnetic compatibility (EMI/EMC) testing
6) **Mission Simulation and Operational Verification**
   - End-to-end communications testing with simulated multi-day latency
   - Autonomous Fault Detection, Isolation, and Recovery (FDIR) validation
   - Simulated cruise and science operations using mission timelines
   - Hardware-in-the-loop testing with synthetic Einstein ring image reconstruction
   - Ground station interoperability testing using CCSDS protocols
7) **Launch Site Operations**
   - Final spacecraft functional checkout
   - Propellant loading and leak checks
   - Battery charging and launch configuration verification
   - Launch vehicle integration and interface testing
   - Final countdown simulations and readiness review

III. Ground Stations

A. Hardware, Software, and Handheld Operation Equipment

The SGL mission employs four globally distributed ground stations optimized for infrared optical communications. Unlike traditional RF-based deep space networks, optical ground terminals require clear atmospheric conditions, driving the selection of high-altitude, arid locations:

Ground Station	Longitude (°E)	Primary Advantage
Fucino Space Center, Italy	13.6	European coverage; existing infrastructure
West Australia Space Center	115.4	Arid climate; minimal atmospheric interference
Haleakala Observatory, Hawaii	203.8	Above cloud layer; excellent seeing conditions
Atacama Observatory, Chile	292.3	High altitude; minimal precipitation

Table 9 SGL mission optical ground station network.

The four-station architecture provides the following:

- **Continuous Coverage:** With longitudinal separations of approximately 90°, at least one station maintains line-of-sight to the spacecraft at any given time.
- **Weather Redundancy:** The fourth station (beyond the minimum three required for 24/7 coverage) ensures that localized atmospheric conditions at any single site do not interrupt mission-critical communications.
- **Data Routing:** All stations connect to the MOC via secure terrestrial fiber networks, with automatic handoff protocols as the spacecraft moves between station visibility windows.

Each ground station is equipped with optical terminals capable of both uplink (command transmission) and downlink (telemetry/science data reception) at the mission's specified data rates. Four atmospheric sensors will continually support the ground station during nominal operations. At each site, a weather station, a sunphotometer, a ground scintillometer, and a cloud imager will work as an integrated suite to characterize the optical channel.

B. Antenna Installation

NASA's Deep Space Network (DSN) doesn't currently support optical communication. Having a deep space network to relay communications would mitigate single-point failure risks and would allow a safer transfer of information. Without this network, the necessary architecture will be that of the Direct to Earth (DTE) communications link. Like the name suggests, in a DTE link, the optical laser signal will travel directly from the spacecraft, through space, through Earth's atmosphere, and to the ground station recievers.

At extreme ranges, like the ones this mission will be operating in, this laser link will become very faint and can gain noise. When designing ground stations, it is important to note that larger ground stations will enhance link margins considerably, helping to adjust for the effects of long range communication links. A relevant theoretical design report, working on a similar optical system, performed a trade study on three different ground station sizes, 5-m, 10-m, and 30-m class ground stations. This trade study showed that the 30-m class ground stations are not only favorable, but necessary to enable this deep space connection. The results of this trade study greatly informed the design choice of 30-m class ground stations.

Each of the four 30-m class ground stations will be custom built on sites where ground stations have legacy operations. If possible, modifying pre-existing ground stations to fit the specifications of this mission will be cost and time effective.

C. Setup and Operation

The Mission Operations Center (MOC) serves as the central hub for all spacecraft commanding, telemetry processing, and mission planning activities. Located nominally at the Jet Propulsion Laboratory (JPL), the MOC houses the flight operations team and provides the following capabilities:

- **Command Generation and Validation:** All telecommands are developed, simulated, and validated at the MOC before uplink. Given the 3.75–5.20 day one-way light time during science operations, commands are time-tagged and uploaded as activity blocks rather than real-time instructions.
- **Telemetry Monitoring and Analysis:** Real-time (delayed) telemetry display, limit checking, and trend analysis for all spacecraft subsystems. Automated alerting systems notify operators when parameters exceed predefined thresholds.
- **Mission Planning and Scheduling:** Development of short-term (weekly) and long-term (monthly/yearly) activity plans, coordinating spacecraft modes, maneuvers, science observations, and downlink sessions.
- **Anomaly Response Coordination:** The MOC serves as the decision-making center for anomaly investigation and recovery procedure development.

As the logistics and operations center, the MOC will maintain operations within the Consultative Committee for Space Data Systems (CCSDS) protocols. CCSDS provides the standardized "language" for space data systems, enabling reliable, interoperable communication across missions and agencies, from Earth orbit to interplanetary networks.

IV. Payload Process Design

A. Payload Objectives

The primary goal of the SGL's payload is to collect the faint light from PCb which is amplified by the Solar Gravitational Lens, suppress the light from our sun, and convert the Einstein ring brightness distribution into the image of the target planet. Because of the sun interference, we cannot image the ring directly and process that, we must instead observe the ring over time as the spacecraft flies through the focal region of the SGL, and gather images over time to build into the final image. The focal region of the SGL is between 548 au and 950 au, however for our current imaging technology, we would have effective imaging only between 650 and 900 au [3]. The ultimate objective of this spacecraft is to produce 3D Hyperspectral Images, or a hyperspectral data cube using two spatial dimensions and one spectral dimension. This product allows us to analyze the target planet, and gather information on its atmospheric make-up, surface characteristics, and potential for habitability through life signatures.

B. Signal Improvements & Image Integration

While the coronagraph is used on board to suppress the solar disk that interferes with the ring, the major source of noise is actually from the solar corona, which cannot be blocked by the coronagraph for most of the mission [4]. This is because the corona separates from the sun as a function of distance, and will overlap with the Einstein ring during the early stages of the science phase. At 650 au when the science begins, there will be large amounts of interference

from the corona, and after ~ 100 au, this separation will grow from the statically placed ring, and the interference on the image processing will decrease dramatically. We utilize a coronagraph with a high suppression value in order to minimize long term, constant interference to the ring.

The primary method for minimizing the interference of the corona is to image the ring within the mid-IR light spectrum. This is because the solar corona is found to be quieter within this IR spectrum, and planets are self luminous within this wavelength, allowing for a much higher Signal to Noise Ratio (SNR) [5, 6]. The estimation of the SNR for a 1 m telescope is described in detail using S.G. Turyshev and V.T. Toth's methods for deconvoluting spectrally resolved images [4], for our purposes, we use the following equation for the total SNR after integrating over pixel area, bandwidth, and time:

$$\mathrm{SNR}(x_0, \Delta t, \Delta\lambda, A) = \mathrm{SNR}(x_0, x_i, t, \lambda)\,\sqrt{A_{\mathrm{pix}}\,\Delta\lambda\,\Delta t}. \tag{1}$$

Where x_0 is the telescope position in the SGL image plane, x_i is the position of a pixel on the focal plane, λ is the wavelength (3 to 50 μm for mid-IR), t is time, A is the detector integration region, A_{pix} is the area of one detector pixel, $SNR(x_0, x_i, t, \lambda)$ is the local SNR density per unit detector area per unit wavelength per unit time. With this equation, we can achieve a SNR pre-deconvolution of 55 for a 1024x1024 pixel production in $\tilde{9}.5$ years, just within our science phase window, after an integration time of 277.7 seconds per pixel.

The caveat of this SNR is the deconvolution and reconstruction of the image. The next equations will calculate the deconvoluted SNR and show that at the megapixel level, the integration time needed causes the SNR to drastically drop, leading to ineffective imaging. Because deconvolution amplifies noise, Turyshev and Toth estimate the resolved SNR (SNR_R) to be:

$$SNR_R \simeq 0.891\,\frac{D}{d\sqrt{N}}\,SNR_C \tag{2}$$

where

$$D_{pix} \simeq \frac{2zR_\oplus}{z_0 N} \tag{3}$$

D is the image-plane pixel spacing, $R_\oplus$ is the diameter of the sun, d is the telecope apeture, N is the number of image pixels, and SNR_C is the convoluted SNR. Using $N = 1024 \cdot 1024$, $SNR_C = 55$, $z_0 = 1.3pc$, $z = 650au$, and $d = 1m$, we achieve a pixel spacing of 30.2 m, and a deconvolution SNR of 1.45. Clearly, this value is disappointing, and this comes from the high penalty factor of SNR_R, as a result of the large pixel quantity. By dropping our expected pixel quantity to 512x512, or 256x256, we can improve our SNR greatly. The following table gives SNR_R values for each of these pixel quantities, integrated over a 1, 3, and 9 year data collection phase.

Table 10 Estimated reconstructed SNR for different image resolutions and observing times.

Image size	**Total pixels**	D	T	**Adjusted** SNR_C	SNR_R
256×256	65,536	120.8 m	1 yr	73.3	30.8
256×256	65,536	120.8 m	3 yr	127.0	53.4
256×256	65,536	120.8 m	9 yr	220.0	92.5
512×512	262,144	60.4 m	1 yr	36.7	3.85
512×512	262,144	60.4 m	3 yr	63.5	6.68
512×512	262,144	60.4 m	9 yr	110.0	11.6
1024×1024	1,048,576	30.2 m	1 yr	18.3	0.48
1024×1024	1,048,576	30.2 m	3 yr	31.8	0.83
1024×1024	1,048,576	30.2 m	9 yr	55.0	1.45

It should be noted, that given the spare margin in our OBC and the reserved storage that can be held on board, it would be trivial to run multiple pixel resolutions at the same time, allowing us to simultaneously deconvolute both ranges of SNR and their opposing resolution.

C. Hardware & Software Protocols

The Payload Optical train uses a 1 m JWST-style folded telescope, where incoming light reflects off the primary mirror into the secondary, which reflects into the primary optical path. The design uses a 1.2 m focal-length with an effective focal length of 10 m at the coronagraph. The science path includes an Internal Lyot Coronagraph which suppresses solar disk light before the path reaches the detector. The baseline required solar-suppression should be approximately 10^-6 solar suppression, however a suppression of 10^-7 is ideal given time for future advancements to the small scale high quality coronagraph such as the Roman Telescope [7]. A polarizer or polarimetric filtering element should be included to support the required solar light rejection needed to improve the image processing. The detector we use for light capturing is a Charge-Coupled Device (CCD) based hyperspectral detector, which is an imaging system that uses a charge-coupled-device focal plane. We image the ring with a spectral range of 0.5-1.5 μm, and a minimum of 200 spectral channels. On the Software side, the payload should time-stamp and digitize measurements, then pass the partially processed science data to the OBC for proper reconstruction.

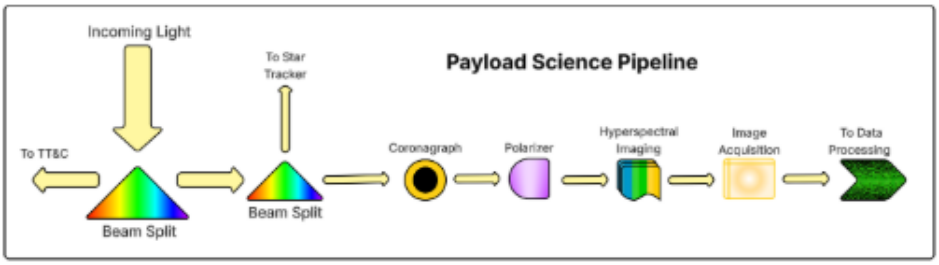

Fig. 2 Science Pipeline Diagram

D. Power & Data Needs

The payload must remain within the strict 10 W power allocation, and stay under 20 kg in order to meet the mission mass requirements. This is the governing payload constraint, and all decisions on the pipeline have been made to account for these requirements. The data system requires approximately 1 TB of onboard active storage dedicated in the OBC, which is continuously autonomously organized for compression, reconstruction, verification, downlink scheduling, and discarding of raw measurements. The image reconstruction itself is GPU-accelerated and staged, using a dedicated reconstruction processor to generate coarse products first and refine higher-resolution regions as additional measurements and compute time become available. This allows the OBC to return early image products for downlink while continuing to improve higher-resolution construction over time.

E. Interfaces, Processing Flow, & Downlink Approach

The payload interfaces optically with the ADCS and TT&C subsystems through beam-splitters in the telescope path. The incoming light is rerouted to ADCS for pointing and attitude feedback, as well as to startrackers, and another route is to the TT&C optical acquisition and is used to receive uplink data from Earth. The remaining science light is then routed through the coronagraph, polarizer, hyperspectral detector, and others for data collection. The processing flow begins with the detector converting the optical light into digitized, time-tagged science measurements. These measurements are sent through the payload interface on the OBC where the data is staged for reconstruction. The OBC stores recent raw science products, and discards previous raw inputs to save space. New data validates previously reconstructed layers, and adds to the overall processed image of the target planet. The downlink for this subsystem follows from the OBDH, and it is sent to the TT&C subsystem. See those respective sections in this paper for details on the downlink.

V. Propulsion

A. Requirements & Trade Study

1. Requirements

The main goals of the propulsion subsystem are to:

- Provide the necessary ΔV's needed for the mission,
- Ensure that the craft stays under 16,800 kg,
- Ensure that the craft can fit within a 13.2 meter tall cylinder with a diameter of 5.2 meters,
- Ensure the propulsion subsystem can survive high amounts of thermal and ionizing radiation,
- Ensure that the propulsion subsystem is reliable and minimizes the risk of the mission,
- And minimize the technological advancement needed.

Using Ansys Systems Tool Kit (STK), we were able to find the ΔV required to perform each maneuver. (More explained in section XII) These numbers can be improved upon with further enhancement to the mission architecture and types of maneuvers.

GEO Escape	12.5 km/s
Jupiter Oberth	3.6 km/s
Solar Oberth	41.6 km/s
Spiral after 650 au (axial)	4.8 km/s

Table 11 ΔV budget during each stage of the mission

2. Propulsion Mechanisms

To achieve these goals, four separate propulsion mechanisms were taken into consideration.

First, a standard methalox bipropellant thruster is looked at it. Bipropellant mechanisms are common in many missions, and this mission is no different. The main benefit of bipropellant is that it can provide a significant amount of thrust while needing very little electrical power. This makes it useful in situations where we need a large burn where solar panels are not effective. Methalox was chosen due to it being already technologically viable while providing a surprisingly high specific impulse despite its average structural coefficient.

The second mechanism is hydrazine mono-propellant. Mono-propellant, due to needing only one tank to store its fuel, has an extremely low structural coefficient. Along with its decent thrust and proven radiation and thermal tolerance from its use in the Voyager missions, it is perfect to use in deep space environments such as far in the heliosphere.

The third mechanism is ion thrusters. These are extremely appealing as they have specific impulses 5-10 times higher than standard chemical rockets. Since the mission requires large amounts of ΔV, this tool is crucial to minimizing the mass of the system. They have also been proven to be quite resilient as NASA's Dawn mission used ion thrusters to go through the highly energetic regions between the moons of Jupiter.[8] The only problem is that they require large amounts of electrical power and have little thrust, which limits where they can be used.

The last and most unique of the mechanisms is the solar sail. The solar sail is a large, thin sheet of reflective metal that uses the light from the Sun to propel itself. The lack of propellant and the ability to make the sail incredibly light allows the craft to gain large amounts of energy for a relatively small mass ratio. However, the sail becomes ineffectively quickly the farther the craft is from the Sun. Additionally, the technology is quite new and still needs further development to reach the readiness required for this mission.

Table 12 contains all the different mechanisms with their relevant information. The section "Reliability" is quite difficult to quantify. It includes how developed the technology is (Technology Readiness Level), how radiation and thermal tolerant it is, its inherent risk of failure, among other characteristics. It's organized qualitatively as "low", "medium", "high", and "unknown". "High" means that it has an almost zero chance for failure and can without a doubt survive high amounts of radiation for a prolonged period of time. "Medium" indicates that it has shown that it can survive high amounts of radiation for short bursts and has low risk of failure. "Low" means that it is sensitive for radiation and has inherent risk in its design. "Unknown" means that not enough research has been done to know.*

3. Architecture Selection

Now that the mechanisms are known, the way the mechanisms are utilized are also varied. Four different methods were identified, simulated, and analyzed.

1. Standard

*The "readiness" of the solar sail is more complex than the number itself suggests. Please take a look at Additional Analyses section of the paper for more details.

Mechanism	Performance Characteristic	Reliability	Technology Readiness Level
Methalox Bipropellant	368s I_{sp}	High	9
Hydrazine	220s I_{sp}	High	9
BET-300-P Config. B Ionic Propulsion[9]	2300s I_{sp}	Medium	9
Solar Sail	1 $\frac{g}{m^2}$ ρ_A	Unknown	3

Table 12 Important information of the relevant propulsion mechanisms

This is the original idea that came to mind when the orbital mechanics was first developed. The method included using Methalox to burn away from Earth and at Jupiter since the craft is far from the Sun and those burns require high thrust and ΔV. Then, once close to the Sun, the solar sail is deployed to gain a large amount of energy and then detached at 30 AU. On the way to the imaging spiral, path correction burns are necessary. Hydrazine was picked for this purpose as it has shown to be extremely reliable. Ion propulsion was also considered but it has not been stress tested to such a degree, therefore introducing a factor of unreliability. Thankfully, the low ΔV for correction burns means ion propulsion is not necessary to keep within mass constraints. However, the imaging spiral is a low thrust maneuver that requires a large amount of ΔV, so ion propulsion there is necessary to keep the craft under the mass limit.

This method is reasonable and works well, but other modifications were considered that could potentially reduce mass, or reduce the complexity of the mission.

2. Pre-Solar Ion Propulsion

The first alternate design used the fact that since the travel time between Jupiter and the Sun is quite long (2 years), and since the craft is relatively close to the Sun, the craft would use solar panels to power high thrust ion propulsion to gain efficient ΔV before the Solar Oberth. However, the increased mass from the solar panels along with the negligible increase in ΔV made this variation nonviable.

3. Post-Solar Ion Propulsion

Similar idea to last, however the burn time is longer after the solar Oberth so hypothetically we should get a significant amount of ΔV and also reduce the time to get to the imaging plane. This reduction in time adds onto the increase in ΔV, theoretically reducing the size of the sail at the Oberth.

However, when simulated this turns out to be wrong. Using the most advanced ion propulsion system, the NASA Evolutionary Xenon Thruster (NEXT)[10], the increase in mass for the generator outweighs the reduction in solar sail size. Also, the increase in mass means that although the area to mass ratio for the sail is dropping, the actual area of the sail is increasing. Additionally, when the ion prop eventually stops, the insane excess of energy will lead to electrical and thermal issues during imaging. These results are calculated for different thrust powers and burn times and graphed in figures 3a and 3b.

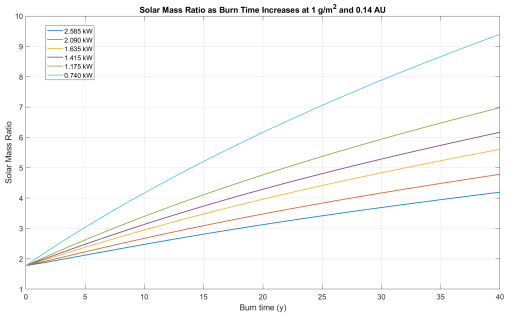

(a) Mass ratio from the solar Oberth and ion burn as the length of the ion burn increases. Notice that the longer the burn, the larger the mass ratio.

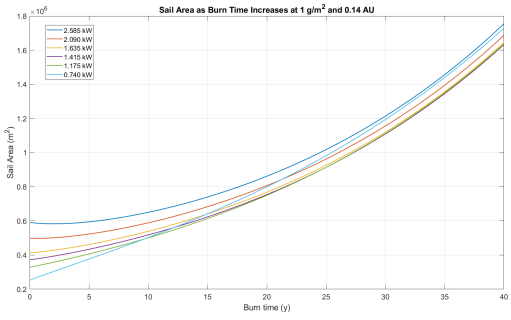

(b) Sail size as length of the ion burn increases. At high powers, the sail does decrease in size slightly, but the increased complexity and mass is not worth it. The lower powers are ineffective completely.

4. Aided Solar Oberth:

The idea of this method is to lean into the benefits of an Oberth and to use a chemical burn at perhelion along with the sail. The hope is that we can reduce the size, and therefore the technological level required, of the solar sail without

increasing the mass of the craft too heavily.

Although the size of the solar sail does decrease when aiding it with a methalox rocket, the mass increase and complexity is too drastic to be useful. The results are graphed in figures 4a and 4b.

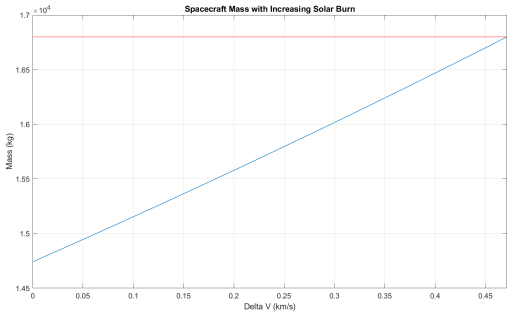

(a) Total mass of the craft as we increase the ΔV from the methalox rocket in the aided solar Oberth. Notice that the mass does increase drastically, with the graph stopping at the hard limit of 16800 kg as shown by the red line.

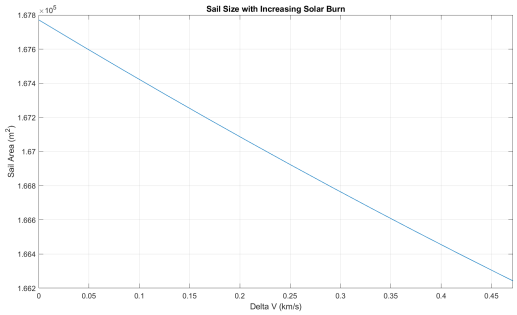

(b) The size of the sail as we increase the ΔV from the methalox rocket in the aided solar Oberth. Notice how the sail size does decrease, but the decrease is insignificant in affecting the technological requirement for the mission.

5. Conclusion

Despite the standard approach being the first we thought about, it turned out to be the most effective one we analyzed. There are other ideas such as not using the Sun but instead taking a path similar to Voyager, but that would delay the launch date to be in the far future and have their own issues regarding imaging.

B. Sizing & Safety

What is great is that the "standard" architecture is able to follow the hard constraints of the mission, although the high technological requirement from the large solar sail leaves much to be desired. The sizing of all the propulsion components are shown in table 13. Note that stage 1 does not include the fuel used by Destiny's carrier rocket that gives the craft an initial boost towards Jupiter.

Regarding safety, the structural coefficient of 0.08 applied to the methalox rocket ensures that the tanks are strong enough to allow the safe storage of high pressure fuels. Hydrazine and ion propulsion can also be designed to be extremely low risk. They are not that relevant to the total weight of the craft and therefore can have a high factor of safety when designing their structure without increasing the weight too much. The only high risk operation is the unfolding of the solar sail, which leads to some rotational instabilities and overall difficulty trying to open the thin sail without tearing or unnecessary folding. This is part of the technological requirement of the sail.

VI. Communications Subsystem

A. Communication Requirements

- The spacecraft shall support a science data rate of 16 Gbits/year from 900 au.
- The spacecraft shall maintain down-link data rates with Earth at > 100 bps from distances up to 950 au.
- The ground stations shall maintain up-link data rates that support > 50 bps at 950 au.
- The communications system shall maintain a 24/7 connection with the spacecraft.
- The spacecraft shall have a link margin of greater than 3 dB.

B. Communication Hardware

For traditional near-earth spacecraft, Radio Frequency (RF) is the most common means of communication. Many satellites near Earth or the Moon will use Ka-band RF, between 26.5 - 50 GHz. Further missions, such as the Mars rovers and Voyager 1, utilized X-band RF, at 8- 12 GHz. When designed for the extremes at 900+ au, RF based communication subsystems must become extremely bulky. Additionally, because data rates scale with an inverse-square of distance, the transmission bit rates get unusably slow. To solve this problem, developments in optical (laser) communications at

Prop Component	Weight (kg)	Size (m^3)
Stage 1: Takeoff from GEO		
Lox	10038	8.8
LCH4	2641.5	6.26
Structural	1103	1.2
Stage 2: Jupiter Oberth		
Lox	479.63	0.42
LCH4	126.22	0.3
Structural	52.68	0.06
Stage 3: Solar Oberth		
Solar Sail	167.8	1.67 (Sail: 410x410 m)
Structural	~0	~0.33
Stage 4: Cruise/Imaging		
Hydrazine	6	~0
Electrospray Ion Thruster	24.4347	0.02
Structural	1	~0
Total		
Total	14714.1 (including dry)	19.06 (prop only)

Table 13 Sizing of the propulsion mechanisms at different stages of the mission.

NASA have become the forefront of deep space data transfers. NASA's recent Deep Space Optical Communications (DSOC) experiment demonstrated a major step forward in enabling reliable deep space communication with laser pulses.

The onboard optical terminal is modeled on NASA's DSOC Laser Transceiver (FLT) architecture with the following parameters: 15 W transmit power, 4.7 kg onboard mass allocation, 1064 nm downlink, and 1550 nm uplink. The photon-counting camera detects the 1550 nm uplink beacon from the ground terminal and recovers low-rate command data. A single detector array simultaneously supports beacon acquisition, closed-loop pointing, and uplink data detection with a avalanche photodiode (APD) array with single-photon sensitivity. The Disturbance Isolation and Pointing Assembly (DIPA) mechanically decouples the optical head from spacecraft vibration, allowing for the extreme required pointing accuracy to be feasible. A beam combiner and beam splitter will direct the uplink and downlink beams through the apertures and interact with the payload subsystem to prevent the beams from leakage. Pulse Position Modulation (PPM) is selected as the modulation scheme because it concentrates all transmit energy into brief, high-peak-power pulses, maximizing photon efficiency. Our 16-ary PPM will split and encode the optical pulses into 16 slots, with 4-bits of information per slot. A master-oscillator power-amplifier (MOPA) architecture is used in the transmit chain. A single-frequency seed laser generates the 1064 nm carrier, and the 16-PPM pulse pattern is amplified. A Ytterbium-doped fiber amplifier (YDFA) then boosts the average output to 15 W into single-mode fiber. When receiving uplink, a photon-counting APD array, a time-to-digital converter (TDC), and a soft-decision forward error correction (FEC) decoder are used to process incoming uplink.

C. Communication Autonomy & Protocols

Onboard systems will be highly autonomous, only relying on ground stations for clock adjustments and ephemeris uploads. Multi-day communication delays will make manual commanding incredibly difficult after reaching 550+ au. Time-tagged commands will be the primary way of initiating events and maneuvers at predetermined times during the cruise. Some examples include the trajectory maneuvers for the Earth-Jupiter transfer, solar infall, and hyperbolic escape. Time-tagged commands will ensure mode transfers align with communication and data acquisition opportunities. Optimal times for science gathering and high-rate downlink will be turned into these timed commands. This highly autonomous system will alleviate pressure from the ground stations to constantly monitor and react to onboard telemetry changes. This allows the staffing requirements to drop to a 8/5 system during nominal conditions. A fleshed out monitoring and alerting system with FDIR triggers will protect the spacecraft and react to dynamic conditions like

battery levels, thermal extremes, or ADCS pointing. Finally, a Safe Mode/Contingency Mode will put the spacecraft into a state of self preservation in the event of a rare mission-threatening event so that ground teams can react to the event and drive key decision making. This retains ultimate mission authority within ground teams and helps mitigate the dangers of a fully automated mission.

D. Link Budget Analysis

Term	Symbol	Value
Transmit optical power	P_{t}	15 W
Wavelength	λ	1064 nm
Transmit aperture	D_{tx}	1.0 m
Receive aperture	D_{rx}	30.0 m
Information bit rate	R_{b}	2640 bps
PPM order	M	16
Code rate	R_{c}	0.50
Beam divergence	θ_{div}	1.298 μrad
Geometric capture efficiency	η_{geo}	6.611×10^{-15}
Pointing loss	L_{point}	0.464 dB
Atmospheric loss	L_{atm}	2.5 dB
Received optical power	P_{r}	−138.1 dBW
Detected signal photon rate	N_{sig}	6.639×10^{4} s^{-1}
Detected background photon rate	N_{bkg}	7.523×10^{4} s^{-1}
Signal photons per slot	$n_{\mathrm{sig,slot}}$	3.144
Signal photons per information bit	$n_{\mathrm{sig,bit}}$	25.149
Required photons per information bit	$n_{\mathrm{req,bit}}$	10.0
Optical link margin	$\mathbf{M}_{\mathrm{link}}$	**4.005** dB

Table 14 Photon-counting optical link budget for the 950 au **SGL downlink case.**

VII. Mechanical and Structural Subsystem

A. Design Requirements & Specifications

The Mechanical Subsystem provides the primary load-bearing framework for the spacecraft and must support all other subsystems during launch, solar sail deployment, and the long-duration cruise to the Solar Gravitational Lens focal region. The structure must maintain the alignment of the 1 m primary mirror and deployable 0.25 m secondary mirror at the forward end, support the propellant tanks and propulsion hardware near the vehicle's center, and provide mounting for the sail deployment mechanisms and radiation umbrella at the aft end. During launch, the frame is required to withstand a 10 g axial acceleration acting on a total spacecraft mass of 14574 kg, which corresponds to an axial compressive load of approximately 1.43×10^{6} N. This load must be carried without exceeding the yield strength of Ti-6Al-4V Titanium alloy and without inducing buckling in any of the main structural members. In addition, the structure must provide sufficient bending stiffness to avoid excessive deflections and to achieve an acceptable first bending-mode frequency for compatibility with launch vehicle dynamic requirements, while remaining manufacturable and mass-efficient for a long-duration deep-space mission.

The primary spacecraft bus is a three-stage rectangular prism truss fabricated from Ti-6Al-4V Titanium alloy. In the fully stacked launch configuration, the bus measures approximately 1.5 m × 1.5 m × 11 m. This geometry provides the required internal volume for payload, propulsion, tank, avionics, solar sail, and radiation-shield systems while maintaining a compact and stiff launch configuration.

The rectangular truss layout was selected to provide high bending stiffness along the spacecraft's longitudinal axis

and to distribute launch loads through multiple structural members. Cross-bracing between the primary rails improves torsional rigidity and reduces the risk of local buckling. The minimum required Factor of Safety is 1.4 across all major loading cases, including launch, maneuver, deployment, and thermal loading.

System	Dimensions	Weight
Total bus (all stages)	(1.5 m × 1.5 m × 11 m)	135 kg
Solar Sail	Deployed: (167772 m^2 SA) Housed: (2 m^3)	167 kg
Tanks	(1.5 × 1.5 × 8 m)	1156 kg
Payload	Primary mirror (1 m D × 0.1 m H); Secondary mirror (0.25 m D × 0.025 m H); Analysis equipment (1 m D × 1 m H)	22 kg
Sensors, electrical, OBC	Varied	27 kg
Thrusters	(80 mm D × 80 mm H)	8 kg
Total wet mass	(17.14 m^3)	13284 kg
Total dry mass	(1.5 m × 1.5 m × 11 m)	1288 kg

Table 15 Mass Budget. Estimated mass allocation for the primary spacecraft systems

B. Production Process

Ti-6Al-4V was selected for its high strength, thermal stability, corrosion resistance, and ability to maintain structural performance in the severe thermal environment expected during the Solar Oberth maneuver. These advantages make it more suitable than Aluminum 6061 for critical load-bearing members exposed to high temperatures and large thermal gradients.

Option (Bus frame)	Advantages	Disadvantages	Decision
Aluminum 6061 T6	High heritage, low mass, easy to machine	Higher thermal expansion, lower strength than Ti	Rejected
Titanium alloy (Ti-6Al-4V)	High strength, low thermal expansion, thermal stability	Higher cost, harder to machine, lower conductivity	Accepted
Aluminum-lithium alloy	Lower mass than 6061, good stiffness	Less heritage, higher cost, fabrication risk	Rejected

Table 16 Material Selection. Comparison of candidate bus-frame materials

The tradeoff is increased manufacturing cost and complexity. Titanium is more expensive, harder to machine, and causes greater tool wear than Aluminum 6061. To reduce integration risk, the truss is designed as modular stage assemblies, allowing each bay to be fabricated, inspected, and assembled separately before final stacking.

The telescoping mirror support structure requires tighter manufacturing tolerances than the general bus frame because small alignment errors can degrade optical performance. Mirror deployment rails, guide features, and locking interfaces should therefore be precision-machined and inspected separately before integration with the primary truss.

C. Constraints & Challenges

The most significant mechanical design challenge occurs during the Solar Oberth maneuver at 0.14 AU, where the spacecraft experiences intense solar heating and steep thermal gradients across exposed and shadowed surfaces.

Across these gradients, there is a risk for thermal expansion mismatch between structural members, tanks, pipes, payload supports, and deployment hardware. If no mitigation strategy is implemented, the resulting thermal stresses could cause joint preload loss, structural distortion, misalignment of the telescoping mirror, or localized yielding in sensitive components. In order to account for these challenges, the mechanical design includes compliant and thermally tolerant interface hardware. Belleville washers are used at selected bolted joints to maintain preload during thermal cycling. Their spring-like geometry allows them to compensate for small dimensional changes caused by expansion and contraction, reducing the risk of joint loosening or excessive stress concentration. Flexure joints are used where rigid connections would otherwise transmit large thermal strains into sensitive hardware. These joints allow controlled elastic deformation while maintaining positional constraint in critical directions. This is especially important near payload supports, tank mounts, and long structural members where small thermal strains can accumulate over the 11 m spacecraft length.

The propulsion and fluid routing geometry also includes curved pipe sections rather than fully straight runs. Curved pipe geometry provides compliance against thermal shock and differential expansion, allowing the lines to flex slightly as temperatures change. This reduces bending stress at pipe connections, tank outlets, and valve interfaces. The elongated frame also presents buckling and bending challenges during launch. The 11 m fully stacked configuration must resist axial compression, lateral vibration, and dynamic launch loads without excessive deflection. The three-stage truss architecture addresses this by breaking the spacecraft into shorter structural bays, reducing the effective unsupported length of primary members and improving global stability. Cross-bracing further increases buckling resistance and maintains the rectangular frame geometry under combined axial and lateral loads.

D. CAD

This design distributes axial and bending loads efficiently, provides clear attachment points for the payload, tanks, and thrusters, and offers geometric stability over the mission lifetime. The complete design of all stages is visually demonstrated in Figure 5 below

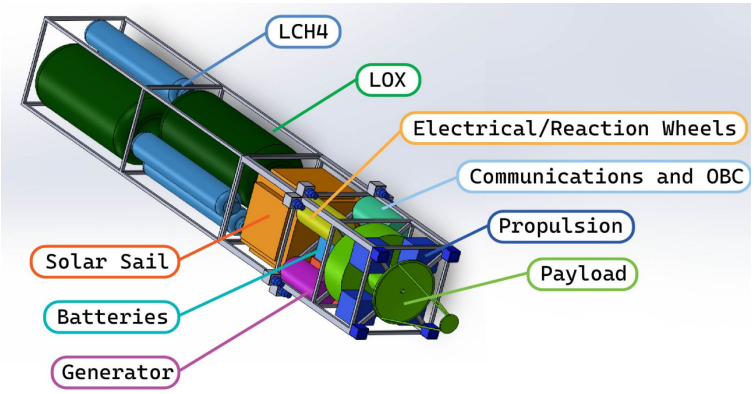

Fig. 5 All stages of the spacecraft

The majority of our volume takes the form of fuel and oxidizer storage, especially in the deployable burner stages. A closer look at just the final stage of our design can be seen in Figure 6 below.

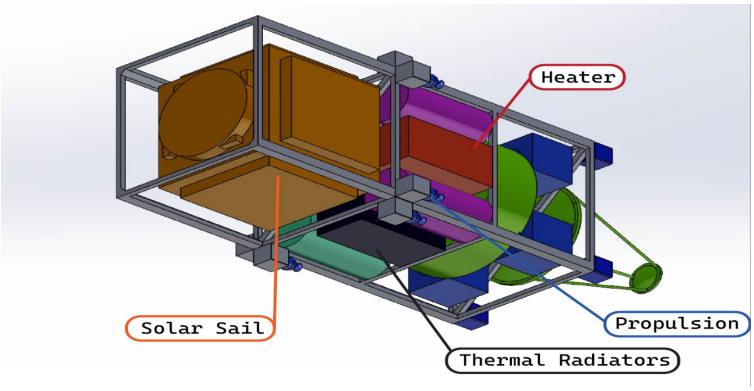

Fig. 6 Final Stage of the spacecraft

The most dominant component in this stage is our solar sail. Even housed in its non-deployed configuration, the sail takes up about a third of the total volume of this stage. When deployed, however, the scale of the solar sail dwarfs the rest of the spacecraft, as an incredibly large surface area is necessary to achieve our desired delta V when leaving the solar system. The final deployed configuration can be seen in Figure 7.

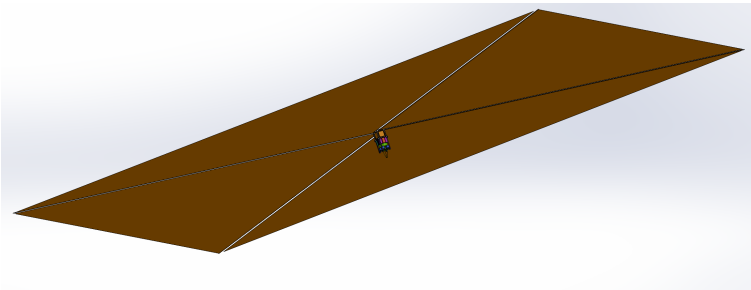

Fig. 7 Final stage with solar sail deployed

VIII. Thermal Subsystem

A. System Overview & Function

The Thermal Control Subsystem (TCS) is responsible for maintaining the spacecraft and its internal onboard electronics within allowable temperature limits throughout all phases of the mission. The function of this subsystem is very important for the Solar Gravitational Lens mission because the spacecraft needs to survive two extreme thermal environments. The first one is intense solar heating during the solar Oberth maneuver in the perihelion phase, and the second one is extremely low external heating during the deep-space cruising phase. The thermal subsystem plays an important role in protecting the spacecraft from overheating or freezing. This includes the structure of the spacecraft, its avionics and payload electronics, and its sensitive onboard data handling hardware. The thermal environment for this mission will be unusually severe because the spacecraft will cover a vast range of heliocentric distances over its lifetime. When the spacecraft is near perihelion, it will be subjected to very high levels of solar irradiance. During the outbound cruise to hundreds of astronomical units, the spacecraft will not experience any absorbed solar heating. So, the spacecraft must rely primarily on insulation, internal waste heat, and supplemental heaters to remain within the acceptable operating limits. These two environments define the bounding hot and cold cases used in the thermal analysis.

In an attempt to address these challenges, our selected thermal architecture will be a hybrid system that will be predominantly passive, but also supported by some elements of active heating when required. The passive thermal control is provided through the use of a perihelion heat shield, multilayer insulation (MLI), surface optical properties that are tailored specifically for thermal control, and the use of dedicated radiators for heat rejection. Active thermal control will be provided through trim heaters during the deep-space cruising phase. This will be needed since passive

retention and internal waste heat from the RTG would not be sufficient to maintain the allowable range of temperatures. In the final design, we give particular attention to the thermal protection of the spacecraft bus and the On-Board Data Handling (OBDH) electronics. This is because the OBDH is very sensitive to temperature and is the most important part of the spacecraft to protect, as the mission would fail without it. Overall, the function of the thermal subsystem is to ensure that the spacecraft remains thermally viable over the full mission by rejecting excess heat in the hot case, retaining sufficient heat in the cold case, and maintaining our critical electronics within allowable temperature limits by using a justified combination of passive and active thermal control elements.

B. Thermal Modeling Approach

The thermal behavior of our spacecraft is analyzed using a first-order, lumped-parameter model that is extended from the steady-state framework into a time-dependent transient simulation. This approach is chosen because it lets us evaluate the evolution of our temperature over time and distance rather than use a model that assumes instant equilibrium. The final thermal model represents the spacecraft using a two-node system that consists of the spacecraft bus and the OBDH subsystem. The bus node represents the bulk structural and external thermal environment of the spacecraft, while the OBDH node represents the thermally sensitive internal component that has strict operating temperature limits. Heat transfer between these nodes is modeled through conductive coupling, and the radiative heat exchange is modeled with heat rejection to space and through internal thermal interactions. The governing equation for energy balance used for each node is expressed as:

$$mc_p \frac{dT}{dt} = \dot{Q}_{in} - \dot{Q}_{out} \tag{4}$$

where m is the effective mass of the node, c_p is the specific heat, and $\dot{Q}$ represents the net heat transfer rate. This formula allows our model to capture transient thermal behavior across all phases of the mission and to approach steady-state conditions dynamically. Our model also included important heat transfer mechanisms. Solar heating is only applied in the hot case, where absorbed solar radiation is:

$$\dot{Q}_{solar} = \alpha S(r) A \eta_{shield} \tag{5}$$

where α is the absorptivity, $S(r)$ is the solar flux at heliocentric distance r, A is the projected area, and η_{shield} is an attenuation factor that represents our heat shield protection, spacecraft geometry, and pointing. For the internal heat generation, the electrical power dissipation from the OBDH, RTG, and other onboard systems is treated as internal heat sources. Our model also takes radiative heat rejection into account. Heat loss into deep space is modeled using the Stefan-Boltzmann relation:

$$\dot{Q}_{rad} = \epsilon \sigma A \left(T^4 - T_{space}^4 \right) \tag{6}$$

where ϵ is the emissivity, σ is the Stefan–Boltzmann constant, and T_{space} is the deep-space background temperature. The model also considered conduction between the OBDH and the spacecraft bus, where it is modeled as:

$$\dot{Q}_{cond} = G(T_{bus} - T_{obdh}) \tag{7}$$

where G is the effective thermal conductance representing structural mounting and thermal interfaces. For the cold case, electrical heaters are activated using a thermostatic control logic:

$$\dot{Q}_{heater} = \begin{cases} Q_{max}, & T \le T_{on} \\ 0, & T \ge T_{off} \end{cases} \tag{8}$$

where Q_{max} is the maximum heater power and T_{on}/T_{off} define the control band. For the simulation, we used two different thermal environments, which are the hot case and the cold case. The hot case represented the spacecraft at perihelion (0.046 au), where solar heating is at its greatest. The simulation evaluates whether the spacecraft can reject sufficient heat to remain within allowable temperature limits. The cold case represents the spacecraft in deep-space conditions near 900 au, where external heating is negligible. The simulation evaluates whether internal heat generation and heater input are sufficient to prevent the spacecraft from freezing. It is important to note that these cases are treated as fixed environmental conditions rather than a continuous trajectory simulation. This is done because it allows for a conservative assessment of thermal survivability under extreme conditions of the mission. The transient thermal

equations were solved using the forward Euler method. At each time step, the heat transfer terms are evaluated, and the node temperatures are updated according to the energy balance. This method provides us with a stable and efficient means of capturing the transient response and equilibrium behavior of the system. The primary assumptions that we made in the thermal analysis are that the spacecraft is modeled as a lumped-parameter system with uniform temperature within each node, heat transfer is dominated by radiation (convection is neglected), thermo-optical properties (absorptivity and emissivity) are treated as constant, the heat shield effectiveness is represented by a lumped attenuation factor, and the subsystem power levels are based on representative operational modes rather than a continuous peak operation. These assumptions are consistent with a first-order thermal analysis and are appropriate for the preliminary design phase of the mission.

C. Thermal Analysis and Results

The thermal performance of the spacecraft was evaluated using two bounding environments that correspond to the most extreme conditions encountered during the mission. These are the hot case at perihelion and the cold case during the deep-space cruise. These two cases provide us with a conservative assessment of the survivability of the spacecraft by ensuring that all of our components remain within allowable temperature limits under worst-case conditions.

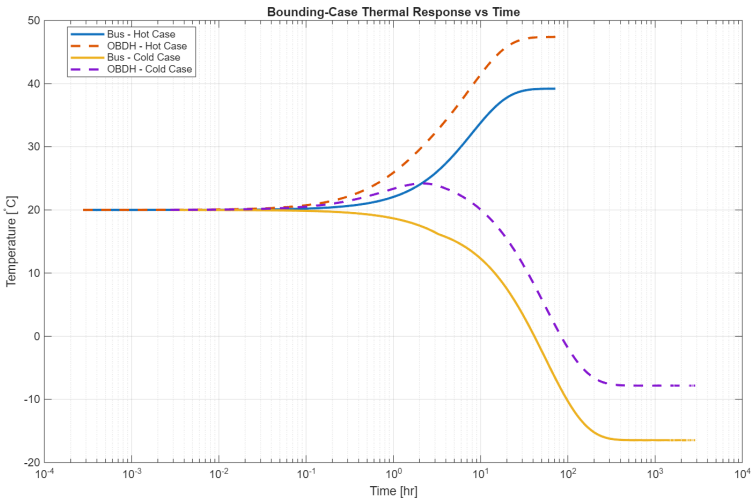

Fig. 8 Transient hot- and cold-case temperature response of the spacecraft bus and critical OBDH node. The hot case assumes a fixed perihelion environment at 0.046 au, while the cold case assumes deep-space conditions near 900 au. The curves show the time required for each node to approach thermal equilibrium under these bounding conditions.

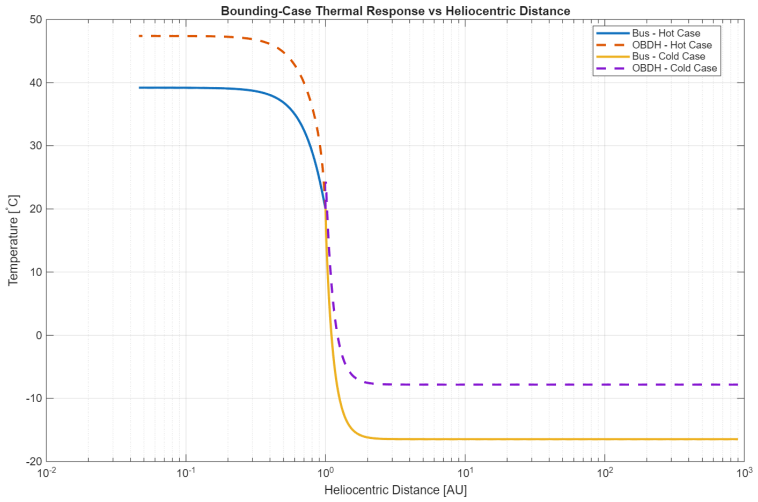

Fig. 9 Bounding-case thermal response of the spacecraft bus and critical OBDH node plotted against representative heliocentric distance. The hot- and cold-case results are shown over their respective distance ranges to illustrate thermal behavior near perihelion and in deep-space conditions. This figure does not represent a continuous trajectory simulation.

The transient thermal response of both the spacecraft bus and the critical OBDH node is shown in Fig. 8 and Fig. 9. The time domain plot illustrates the evolution of temperature towards equilibrium in each environment, while the distance-based plot provides a qualitative visualization of thermal behavior across representative heliocentric distances.

1. Hot-Case Results

The hot case simulation assumes the spacecraft is exposed to the perihelion environment at a heliocentric distance of 0.046 au, where the solar irradiance is maximized. Under these conditions, the spacecraft experiences lots of radiative heat input. This must be balanced by heat rejection through the thermal control system. As shown in Fig. 8, both the bus and the OBDH temperatures increase from the initial condition and then asymptotically approach steady-state values. The maximum temperatures obtained from the hot case are 39.20 °C for the bus temperature, and 47.39 °C for the OBDH temperature. The OBDH node reaches a slightly higher temperature than the spacecraft bus due to localized internal heating being generated by the electronics, as well as its limited ability to perform radiative heat rejection. Heat is conducted from the OBDH to the bus, which then acts as a thermal sink and rejects energy into space. This results in a small, but expected temperature gradient between the two nodes.

2. Cold-Case Results

The cold case simulation assumes deep space conditions near 900 au, where external solar heating is considered to be negligible. In this environment, the spacecraft primarily relies on internal power dissipation and active heater control to maintain the survivable temperature range. As shown in Fig. 8, both of the nodes tend to initially cool from the starting condition and then approach a steady-state equilibrium that is supported by internal heat and heater input. The minimum temperatures obtained in the cold case are −16.47 °C for the spacecraft bus, and −7.82 °C for the OBDH node. The heater system also operates with a peak power of approximately 12 W, which is consistent with our allocated thermal heater budget.

3. Overall Thermal Performance

The results of our bounding-case simulations demonstrate that the spacecraft thermal design can successfully maintain both the bus and the On-Board Data Handling within allowable temperature limits under the extreme hot and cold conditions they encounter. The hybrid thermal control architecture also effectively balances heat rejection and heat retention by using a combination of both passive and active elements of heating. The positive margin for the OBDH demonstrates that the design meets the required performance criteria with a hot-case margin of approximately 2.6 °C and a cold-case margin of approximately 12 °C.

IX. Attitude Determination and Control Subsystem

A. Passive / Active ADCS Design and Simulation

The Attitude Determination and Control System (ADCS) for the Solar Gravitational Lens (SGL) spacecraft is designed to operate in both passive and active modes to support mission phases ranging from solar sail alignment to ultra-precise science pointing. The system architecture combines sun sensors, star trackers, and reaction wheels under the control of the onboard computer (OBC) to maintain accurate and autonomous spacecraft orientation throughout the mission.

1. Passive and Active Operating Modes

During early mission phases and cruise operations, passive sensing through sun sensors is utilized to assist in spacecraft orientation relative to the Sun. This is particularly critical for solar sail alignment, where maintaining the correct attitude relative to solar radiation pressure is necessary for propulsion and trajectory control. Sun sensors provide coarse attitude knowledge and are used for initial acquisition and calibration.

Once the spacecraft transitions into science operations, the ADCS operates in a fully active control mode, relying on high-precision star trackers and reaction wheels. In this mode, continuous feedback control is used to maintain alignment with the focal line of the solar gravitational lens, where extremely small pointing errors can significantly degrade imaging performance.

2. TRIAD Attitude Determination Method

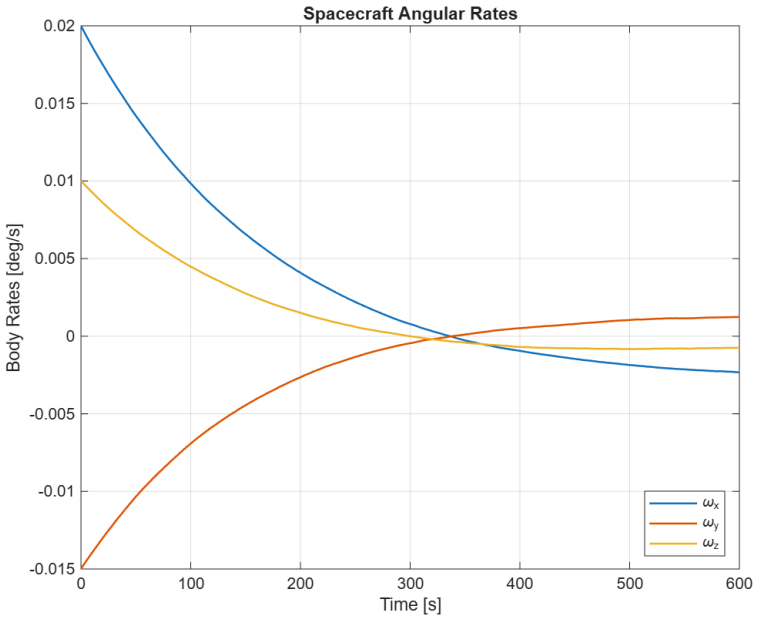

Fig. 10 The simulation incorporates the concept of the TRIAD (Tri-Axial Attitude Determination) method, which utilizes body-frame vectors derived from star tracker centroid measurements. These vectors are compared to known inertial reference vectors from onboard star catalogs to determine the spacecraft's orientation.

In practice, the TRIAD method operates by Identifying at least two known stars in the star tracker field of view, Constructing orthogonal reference frames in both inertial and body coordinates, and Computing the rotation matrix (or quaternion) that aligns the two frames. Within the simulation, this process is simplified into a star tracker measurement update that periodically corrects the estimated spacecraft attitude. Between updates, angular rate propagation using gyro data is used to maintain a continuous estimate. This reflects the intended flight implementation, where TRIAD or a similar algorithm would serve as the foundation for more advanced filtering methods such as an Extended Kalman Filter (EKF).

3. Closed-Loop Behavior

The MATLAB simulation models the full ADCS feedback loop, including Sensor measurement (star tracker and gyro), Attitude estimation, Control computation in the OBC, Reaction wheel torque generation, and Spacecraft rotational dynamics. The system begins with an initial attitude error and angular velocity. The controller computes corrective torques using a quaternion-based proportional-derivative (PD) control law. These torques are distributed to the reaction wheels, which generate angular momentum changes that rotate the spacecraft. Disturbance torques are included to simulate environmental and internal effects. The controller continuously compensates for these disturbances, demonstrating the system's ability to maintain stable pointing under realistic conditions.

B. ADCS Hardware & Implementation

The ADCS hardware selection is driven mainly by our need for high-precision pointing, long mission lifetime, and reliable autonomous operation in deep space.

1. Sensors

The spacecraft utilizes 4 Sodern SED16 Star Trackers which are designed for deep space missions. These Trackers have the ability to provide arcsecond-level pointing accuracy with coming in at just about a total mass of 12 kg and a total power consumption of about 40 W. These star trackers serve as the primary attitude determination sensors during science operations. Their ability to resolve star centroids with high accuracy enables precise alignment with the Einstein ring focal line. In addition to star trackers, sun sensors are used during early mission phases for solar sail alignment and initial attitude acquisition. These sensors provide coarse orientation information and support safe-mode operations.

2. Actuators and Onboard Computer Integration

The control system uses will utilize 4 Honeywell HR04 Reaction Wheels. These will be on board our spacecraft configured in a pyramid arrangement for full 3-axis control. These reaction wheels will be coming in a about 10.5 kg total and a power consumption of 25 W. The pyramid configuration provides redundancy and allows for effective torque distribution across all axes.

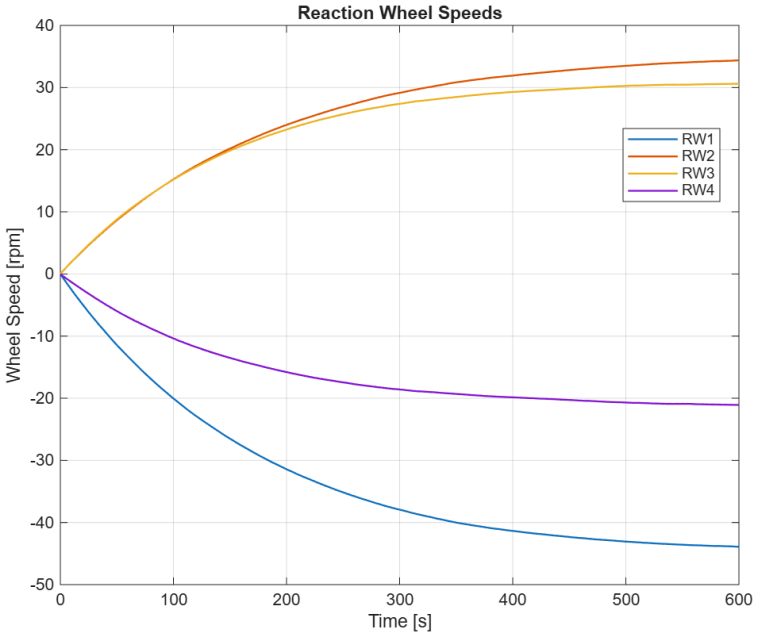

Fig. 11 Reaction wheels generate controlled torques by varying their individual rotational speeds, enabling smooth and continuous attitude adjustments without the use of propellant.

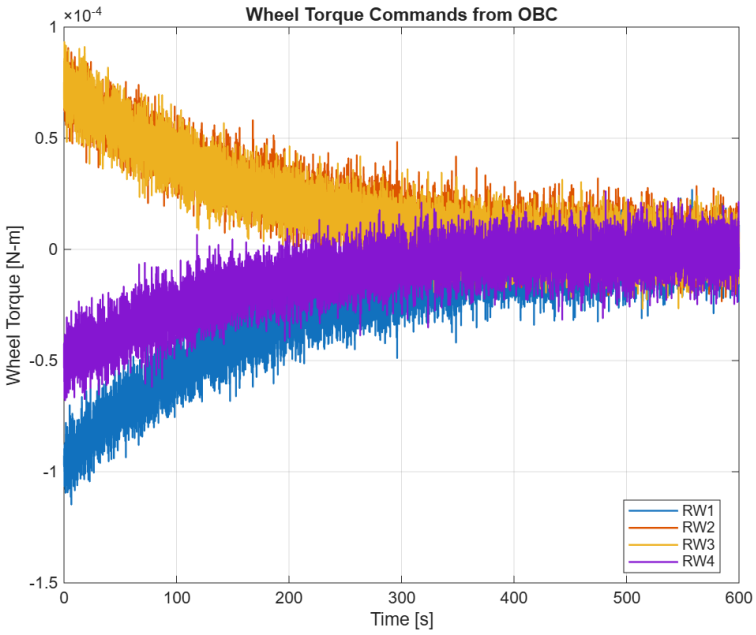

Fig. 12 The On Board Computer (OBC) is in this case is responsible for mainly Processing sensor data, running attitude determination algorithms (e.g., TRIAD-based methods), computing control commands and distributing torque commands to reaction wheels.

Here the system will operate autonomously due to long communication delays at distances up to 900 au. This requires robust onboard decision-making and fault tolerance, as described in our system-level design.

C. Pointing Resolution & Accuracy

Achieving and maintaining precise pointing is critical for the success of the SGL mission. The ADCS must meet a strict pointing requirement of 0.01 arcseconds to ensure accurate imaging of exoplanets using the Einstein ring.

1. Simulation Results: Pointing Stability and Control Effort

The MATLAB closed-loop simulation created demonstrates that the ADCS can reduce initial pointing error over time, stabilize spacecraft angular rates, and maintain a steady-state pointing condition.

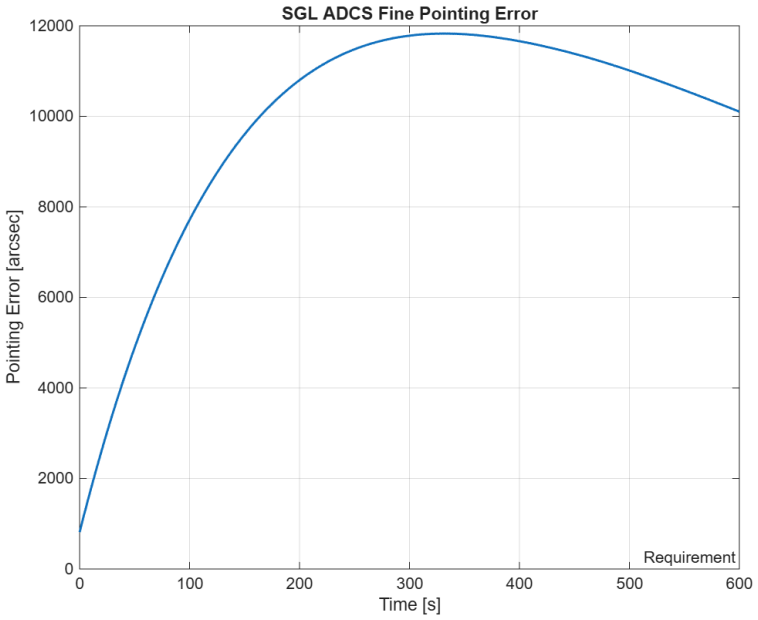

Fig. 13 The pointing error is computed from the quaternion difference between the desired and estimated attitudes and converted into arcseconds. Our simulation results show convergence toward the required pointing accuracy, validating the effectiveness of the control system design.

2. Disturbance Rejection and Sensor Noise Impacts

The simulation also includes constant and time-varying disturbance torques that essentially represent environmental effects. The controller will effectively compensate for these disturbances, maintaining stable pointing with minimal oscillations which could create error. This demonstrates that the PD control law provides sufficient robustness for disturbance rejection in deep-space conditions.

Sensor noise here is introduced in both the star tracker and gyro measurements. The simulation here shows that the star tracker updates correct accumulated drift from gyro propagation, noise introduces small fluctuations in pointing error, and finally overall system stability here is maintained despite measurement uncertainty. Overall, this highlights the importance of accurate sensor fusion and suggests that, for future ideas, implementing advanced filtering techniques would further improve performance.

Our goal with the ADCS subsystem design is making sure it can integrate passive and active sensing with reaction wheel control to achieve the high pointing accuracy required for the SGL mission. The MATLAB closed-loop simulation demonstrates that the selected architecture is capable of stabilizing the spacecraft and maintaining precise orientation under disturbance and noise conditions. While the current model uses simplified assumptions, it provides strong validation of the ADCS concept and establishes a foundation for future refinement, including advanced estimation algorithms, detailed hardware modeling.

X. Electrical Power System

The EPS must manage the energy storage, power distribution, and conditioning. For a long deep space mission (57+ year duration) beyond the solar system, the functionality of solar panels becomes exponentially inefficient as the space-craft strays from the sun. Due to this circumstance, EPS must rely on nuclear power as its main source of power, such as Radioisotope Power Systems (RPS) [**?**]. Nuclear power within a limited weight requirement will produce a minor amount of power, requiring systems to be adjusted to be as efficient as possible. Combined, the systems will be constrained to a peak load of 90 Watts End of Life (EoL), with power switching from Propulsions to OBC after the flight path is managed. It also provides waste heat, which can be harnessed to regulate the temperatures of the main payload systems. [**?**].

A. Main Components & Functions

The main power source will consist of Radioisotope Thermoelectric Generators (RTGs) [**?**], while having a redundant storage system using Nickel-Hydrogen batteries, and a Power Control Unit (PCU) maintaining a 28 Voltage DC regulated bus. The particular RTG used in this design will be the Atomic Planar Power for Lightweight Exploration (APPLE) RTG. This RTG is a completely modular tile-based generator weighing only 200 grams and producing 1.7 Watts-per-tile, utilizing small amounts of Pu-238 surrounded by Platinum and Skutterdite (SKD) thermoelectric converters. This tile-based design allows the ability to spread the tiles in a configuration which utilizes the waste heat to warm major systems within the spacecraft. It also reduces mass usage, being incredibly efficient for its mass, with the ability to reach optimal Beginning of Life (BoL) conditions. The natural decay of plutonium as well as the mechanical efficiency of the thermoelectric converters must be accounted for when reaching EoL conditions. combines, these factors result in a 1.6% annual rate of decay throughout the mission. Accounting for this, the RTG must support 233 Watts BoL, resulting in a total of 137 Tiles that amount to 24.7 kg.

B. Design Drivers

The key design drivers of the mission to be met consist of managing continuous DC power throughout the entirety of the 57+ years, Maintain a positive energy balance at all stages, support peak loads and maintain high-reliability and autonomous operations. This lies in the mission duration and the distance it holds from the sun. The Solar Gravitational Lense is required to be placed at its closest 650 au from the sun. A solar array will be rendered unusable soon after the spacecraft leaves the solar system, which must be accounted for. The full duration of the mission will exceed 57+ years. The RTG design is chosen because of its proven ability to survive for a long period of time and its continuous power generation for a low-power spacecraft. The isotope Pu-238, has a half-life of 87.7 years, and the mechanical efficiency reduced effectively by .8% per year, the overall efficiency will be 1.6%. This means the spacecraft will maintain 90 Watts throughout the mission time of 57 years, with peak power supported through the travel time of 47 years and during downlink events. These constraints are also key to the selection of the Nickel-Hydrogen batteries, with a vast cycle time of 15000+[**?**].

C. Functional Requirements & Selection Criteria

The APPLE-RTG is chosen as the final design due to its light weight mass and versatile applications, supporting 233 Watts of power with a weight of only 24.7 kilograms compared to the MHW-RTG being 37 kilograms. Though a risk that should be considered is the phase of this technology currently. In research phase, it must meet commercial application by the time of launch, though a very well-developed project.

Table 17 RTG Trade Study

RTG Option	Advantages	Disadvantages	Decision
MHW-RTG	Maintains optimal bus power for mass (37 kg, 157 W BoL); Legacy part	Lacking modular design; older model with lower efficiency	REJECTED
8 GPHS-STEM RTG	Modular design; meets optimal power requirement; lower mass (28 kg, 205 W BoL)	Larger model; difficulty with compaction	REJECTED
APPLE-TILE RTG	Modular design; lightweight mass-to-power ratio; can utilize waste heat	Newer technology; still in research phase	SELECTED

D. Energy Storage Budget

DC converters, mechanical switching systems, and shunt regulators will be used to control bus voltage. We will use 28 V DC as the optimum regulatory voltage throughout the bus, as has been historically proven in NASA missions such as Voyager and Pioneer. The spacecraft will use a modular storage design comprising a Nickel-Hydrogen (NiH_2) cell system to buffer transient loads and provide power stability during load-switching events. There will be 23 cells in series, as NiH_2 is 1.25 V/cell. Conservative depth-of-discharge (DOD) and cycle times are chosen via NASA design standards. In this case, to reach 15,000+ cycles, the battery will be limited to 40 percent DOD maximum. This will include a built-in power conditioning unit (PCU) to provide control electronics for the EPS. Shunt and DC regulators

previously mentioned will be implemented to control output voltage and load isolation. Protective elements such as fuses and relays will be installed as well.

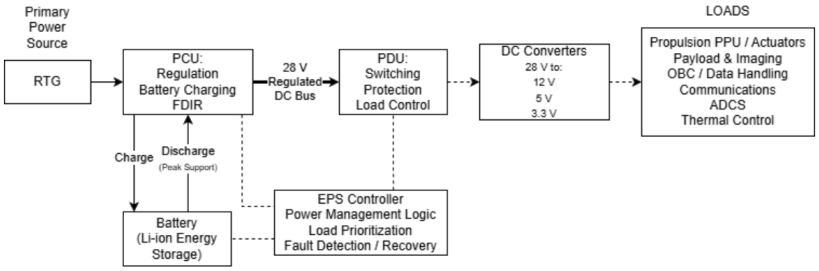

Fig. 14 Diagram of EPS subsystem Link

E. EPS Integration Design

- Provide power generation/consumption simulations over mission timeline (sunlight/eclipse, duty cycles). The spacecraft is RTG-powered; therefore, electrical generation is independent of solar illumination and eclipse does not reduce P_{in}. Eclipse effects are limited to potential increases in electrical load (e.g., thermal control/heaters), which would reduce energy margin. The worst-case power event (downlink at 90 W) is evaluated at EoL and still satisfies $E_{in} - E_{out} \geq 0$ over the 24-hr cycle. The worst-case electrical event considered is a downlink segment at 90 W for 0.5 hr. At EoL, $P_{in} \approx 92$ W so there is no power deficit throughout all operation phases. Taking into account downlink over 0.5 hr, the depth of discharge is calculated to stay at Zero, keeping the battery as a safety contingency to reduce risks. Therefore, the battery provides large margin for transient peak events and contingency operations, while the RTG supplies the long-term average power required for multi-decade cruise.

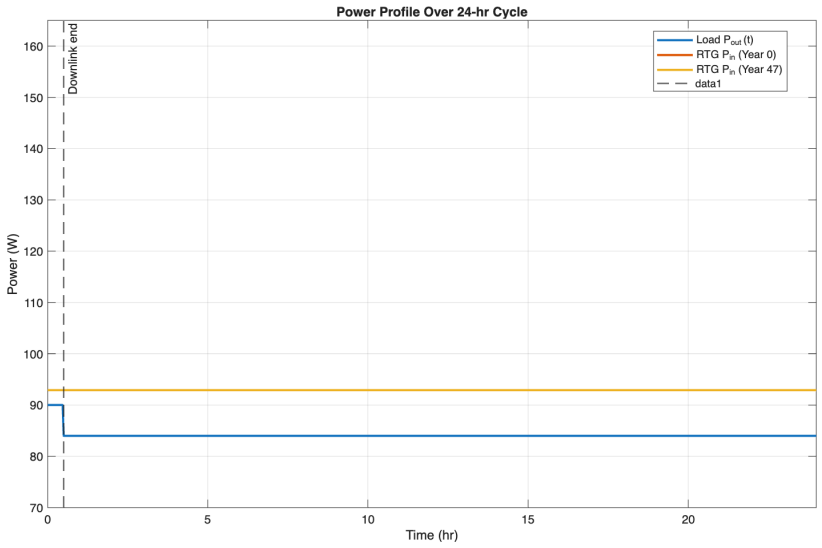

(a) Power loads over 24 hr cycle

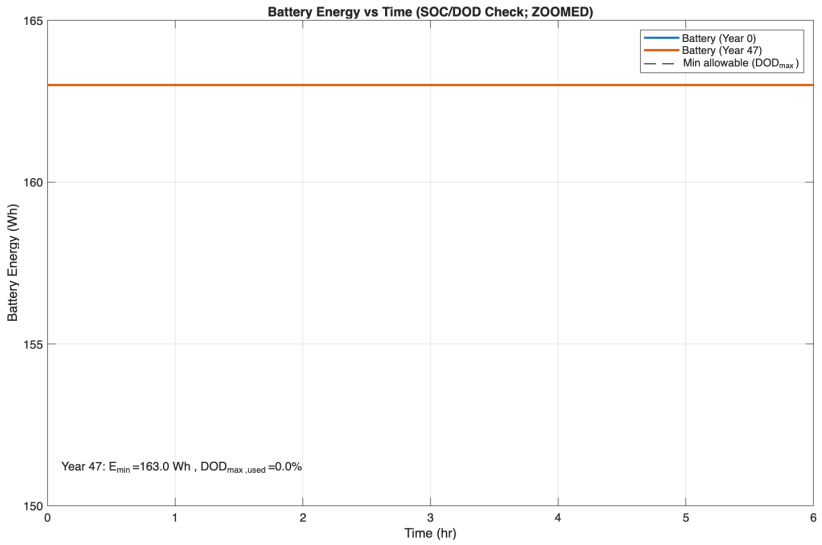

(b) Battery energy vs. Time capacity

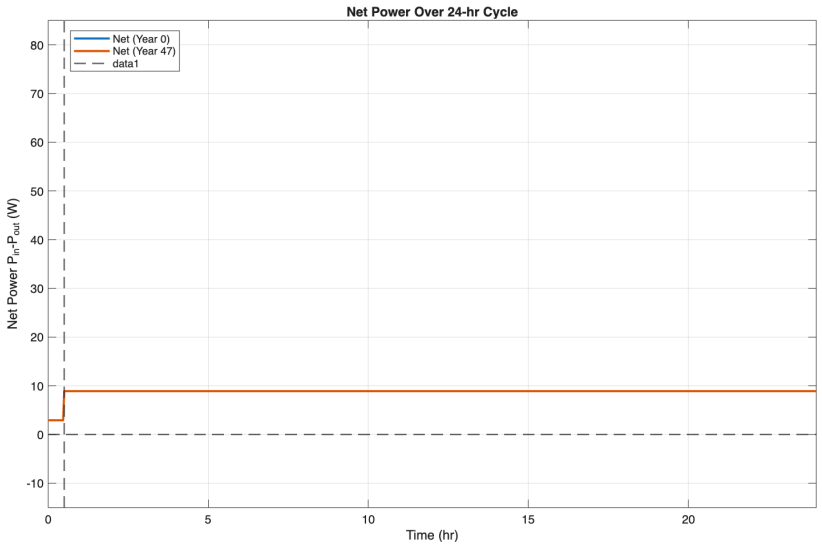

(c) Overall Power production

Fig. 15 Main Electrical Power demonstration over 24 hours

XI. On-Board Computer & Data Handling

A. System Overview and Function

The On-Board Data Handling (OBDH) subsystem's main purpose is to collect, process, and organize all necessary data on board the spacecraft. It interacts with all subsystems through computation, commanding, telemetry, and tracking. The flow path of the OBDH can be broken into three parts, Housekeeping telemetry, Payload science, and Command/uplink flow. The housekeeping telemetry includes EPS, Thermal, Propulsion, ADCS, TT&C, and FDIR. These are all routed through the SP0-S computer, where the OBDH validates the data, time-tags it, compares it to limits, stores the recent hysteresis in its memory, then formats the data into packets and frames for the downlink. The Payload flow starts with the telescope producing image data, which is processed in the image acquisition phase, then compressed at a 2:1 ratio. This is combined with previous image data, and stored in the mass memory to later be packetizing for downlink. The majority of the memory on board the spacecraft is taken up by the science for long term downlink. Finally, the command/uplink flow receives ground Telecommands through the TT&C subsystem, decodes, authenticates, and routes the data to the relevant subsystem. The OBDH stores and schedules time-tagged commands, performs clock adjustments, and adjusts limits autonomously due to the long travel time of information.

This subsystem requires that it will be able to; Process and transmit all housekeeping data, including electrical output, ADCS states and needed adjustments to pointing, payload image processing, and uplink/downlink handling. It should also be capable of calculating required thrust magnitudes to obtain necessary positioning during the transfer phase, and the stellar wobble adjustments during the Payload and Science phase [1]. All data required for future analysis, computation, or otherwise will need to be processed and stored, especially image processing, since previous iterations of the imaging are kept for reference within the algorithm. The OBDH must also receive, process, and execute any commands sent from ground stations, keep track of timing and automation, and identify issues on-board such as faults, which may need to be repaired autonomously.

In order to perform all of these requirements, the OBDH will have the following operational specifications; A processing power of approximately 36 MHZ, derived from the maximum bit rate of 12 kbps and estimating 300 operations per bit. The spacecraft requires a minimum 100 MB of ram for the image processing, and roughly 10 GB needed for the bus, therefore a margin is assumed and 16 GB of ram will be required for the mission. This will be in addition to 1 TB of non-volatile memory to hold the downloaded information from uplink and to protect the system from radiation. There will be a number of time-tagged commands that must be performed at at any given time for the use of maneuvers, propulsion adjustments, deployments, etc. As a result, we require a time-tagged command storage of 10 to hold the data for these on standby.

The central bus computer chosen is the Aitech Defense Systems SP0-S, which is a radiation tolerant cPCI computer. This computer has a high speed processor, is very lightweight, and has a high radiation tolerance which will be required given the extreme environments [11]. The storage space for this computer is estimated to be roughly 3.845 TB minimum, given the incoming data, the processing times, and the length of each of the data phases. Therefore we round up and assign the Mass memory 4 TB of space. The following table provides the summary of the requirements needed for the OBDH subsystem. Fault handling is implemented through a combination of autonomous Failure Detection, Isolation, and Recovery (FDIR) processes, RTOS, hardware watchdogs, telemetry monitoring, and redundancies. Common housekeeping utilizes the SP0-S bus for low rate communication with EPC, Thermal, Propulsion, etc., while SpaceWire is used for the TT&C communication and exchange process [12].

XII. Operations

This section defines the operational architecture for the *Destiny* SGL mission from launch through end-of-life. The 57-year duration and extreme distances (up to 900 au) require high onboard autonomy, as round-trip communication delays reach ~10.4 days at end-of-mission.

A. Concept of Operations & Timeline

The mission comprises seven phases, summarized in Table 19.

Phases 1–3 cover departure through Jupiter. The methalox bipropellant system (368 s I_{sp}) provides the GEO escape and Jupiter Oberth burns, after which Stage 1 and Stage 2 boosters are jettisoned. The Jupiter flyby at 1.2 Jupiter radii perijove redirects the orbital plane toward the anti-Proxima Centauri b direction and is executed autonomously due to the ~45-minute one-way light time.

Characteristic	Requirement
P_{cpu}	5 MHz
M_{RAM}	16 GB
M_{NVM}	1 TB
M_{MM}	3.845 TB
T_{HK}	8 hours
N_{TC}	10 commands/sequences
Central Bus Type	SP0-S
R_{bus}	20 Kbps
ρ_t	4 kRad
link/interface to TT&C	SpaceWire
T Range	-20 to 50 $^{\circ}C$

Table 18 List of Different Requirements for SGL Mission's OBDH

Table 19 Mission phase summary.

Phase	**Dates**	**Duration**	**Key Events**
1. Launch & GEO Escape	Feb 2049	Days	Falcon Heavy; methalox burn ($\Delta V \approx$ 12.5 km/s)
2. Earth–Jupiter Transfer	2049–2054	~5 yr	Heliocentric cruise; TCMs; instrument checkout
3. Jupiter Oberth	~2054	Days	Powered flyby + plane change ($\Delta V \approx$ 3.6 km/s); stage drop
4. Jupiter–Sun Transfer	2054–2056	~2 yr	Inbound coast; thermal-protection config.
5. Solar Oberth & Sail Deploy	~2056	Weeks	Perihelion burn at 0.14 au ($\Delta V \approx$ 41.6 km/s); sail unfurl
6. Interstellar Cruise	2056–2096	~40 yr	~80 km/s coast; sail jettison at 30 au (~2058)
7. Imaging Spiral	2096–2124+	≈10 yr	650–900 au science

Phase 4 is an inbound coast to solar perihelion. As solar flux increases, the deployable heat shield is positioned and thermally sensitive components are stowed.

The thermal control system must keep the spacecraft within its 16–45°C operational range.

Phase 5 is the highest-risk event: a 41.6 km/s Solar Oberth burn at 0.14 au, where irradiance is ~50× the 1 au value. Following perihelion egress, the 410 m × 410 m Aluminized CP1 solar sail (167 kg) is deployed, providing supplemental ΔV via solar radiation pressure.

Phase 6 spans the 40-year cruise. The sail is jettisoned at ~30 au (~2058) when radiation pressure becomes negligible. The spacecraft enters a low-power quiescent state powered by the APPLE-tile RTG (233 W BoL, ~90 W EoL at 1.6%/yr degradation). Periodic instrument calibrations and TCMs continue; communication transitions from X-band to the DSOC-derived infrared laser terminal (15 W, 1064 nm downlink) as range increases beyond DSN RF limits.

Phase 7 begins at 650 au. The spacecraft executes a slow imaging spiral to 900 au over ≥10 years. The 1 m telescope with internal Lyot coronagraph and polarizer images the Einstein ring, producing one 1024 × 1024 pixel composite every 1.6 years. Processed data is downlinked at ≥16 Gbits/year via the optical terminal to four dedicated 30-m ground stations (Ortuccio, Mingenew-Nangetty, Haleakala, Cerro Chajnantor), coordinated through the MOC at JPL.

B. Modes, Procedures, & State Transitions

The spacecraft operates in five modes. All mode transitions beyond Jupiter are managed autonomously by the OBC's C&DH processor using FDIR logic; the GPU co-processor handles science image reconstruction independently.

Cruise/Safe Mode is the default and fallback state. Non-essential loads are shed; the APPLE RTG sustains heaters and the C&DH processor. The NiH_2 battery (163 Wh, 5.2 kg) buffers transient peak loads at <3% depth-of-discharge. Any unresolved anomaly after three FDIR recovery attempts triggers automatic Safe Mode entry.

Propulsion Mode activates for the three major burns (GEO escape, Jupiter Oberth, Solar Oberth). Burn sequences are pre-loaded and executed autonomously; post-burn, spent stages are jettisoned and the spacecraft transitions to Cruise or Sail Thrust Mode.

Table 20 Spacecraft operational modes.

Mode	Power	Thermal	Pointing	Comm
Propulsion	Peak	TPS engaged (perihelion)	Thrust-vector	Blackout possible
Cruise / Safe	Minimal (≤40 W)	MLI + 12.4 W heaters	Sun-pointing	X-band beacon
Sail Thrust	Moderate	Shield + sail reflective	Sail-normal to Sun	X-band
Imaging	~70 W (science)	Passive radiators	0.01 arcsec (fine)	IR laser (scheduled)
Downlink	~90 W (peak)	Passive radiators	Laser boresight → Earth	IR laser (active Tx)

Sail Thrust Mode is active from sail deployment (~2056) through jettison at 30 au. The four Sodern SED16 star trackers (arcsecond-class accuracy, 12 kg total) and Honeywell HR04 reaction wheels (4-wheel pyramid, 10.5 kg) maintain sail orientation for optimal thrust.

Imaging Mode prioritizes science power (~70 W). The telescope, coronagraph, and CCD detector collect long-exposure frames. The Jetson Nano performs onboard deconvolution and staged image reconstruction, storing data in the 1 TB solid-state recorder at ~22 MB/day.

Downlink Mode is the peak-power state (~90 W). The ADCS slews the 1 m aperture to the computed point-ahead Earth direction (compensating for Earth's orbital motion during the multi-day photon transit). The 15 W laser transmits at 8000 bit/s using PPM encoding. Sessions are pre-scheduled and executed without waiting for acknowledgment, using store-and-forward with error correction (CCSDS protocols). Link margin at 900 au is 3.02 dB per the downlink budget analysis.

C. Operations Checklists

1. Checklist 1: Solar Sail Deployment Sequence

Executed post-Solar Oberth once the spacecraft has receded to a thermally safe distance (≥0.5 au).

1) **Health check.** Verify deployment mechanism telemetry nominal; confirm sail membrane temperature below CP1 deployment limit.
2) **Attitude hold.** ADCS establishes sail-deployment attitude (sail normal to Sun). Confirm angular rates <0.01°/s.
3) **Power config.** Shed non-essential loads; energize deployment actuator bus.
4) **Canister release.** Fire pyrotechnic bolts; confirm lid separation via limit switches. *No-Go if unconfirmed within 30 s → Safe Mode.*
5) **Boom extension.** Extend to 25%, verify symmetric deployment, then command full extension. Confirm membrane tension sensors show uniform loading.
6) **Verification.** Compare measured solar radiation pressure acceleration (accelerometers) against predicted value for the 167,772 m^2 sail area. *No-Go if <50% predicted → partial deployment; downlink diagnostics.*
7) **ADCS reconfig.** Update mass properties and center-of-pressure model; enable sail-angle trim control law. Enter Sail Thrust Mode.

2. Checklist 2: Payload Calibration & Comm-Link Acquisition (650–900 au)

Executed at science-phase entry and before each downlink session.

1) **Star tracker calibration.** Fresh star-field observation; cross-reference with latest ground-uploaded Earth ephemeris. Confirm attitude knowledge ≤ 0.005 arcsec.
2) **Telescope boresight check.** Slew to a reference star near the target line-of-sight; measure and correct centroid offset.
3) **Detector checkout.** Power on CCD; perform dark-frame subtraction and flat-field calibration. Verify noise floor within spec.
4) **Einstein ring acquisition.** Slew to predicted ring bearing; execute spiral scan until ring signal locks on fine-guidance sensor. *No-Go if not acquired after extended scan → Safe Mode.*

5) **Science observation.** Begin long-exposure integration per onboard schedule; Jetson Nano performs staged reconstruction; data stored to 1 TB recorder.
6) **Point-ahead computation.** Calculate Earth's position at signal arrival time (current time + one-way light time of 3.75–5.2 days).
7) **Laser link acquisition.** Activate 15 W laser; slew to point-ahead direction; transmit coded beacon. Begin data downlink immediately (store-and-forward, no acknowledgment wait). Monitor pointing residuals; pause and re-acquire if error exceeds threshold.
8) **Session close.** Power down laser; slew to science attitude; log session summary.

XIII. Simulation Evidence & Technical Standards

A. System Simulation Requirements

1. Payload & OBC

Theory

Gravitational lensing by the Sun maps light from a distant source into a bright annular structure in the image plane. The relationship between the source-plane position and the image-plane position is governed by the gravitational lens equation:

$$\mathbf{y} = \mathbf{x} - \boldsymbol{\alpha}(\mathbf{x}) \tag{9}$$

where $\mathbf{x}$ is the image-plane coordinate, $\mathbf{y}$ is the source-plane coordinate, and $\boldsymbol{\alpha}$ is the deflection angle produced by the Sun's gravitational field.

A natural length scale for this system is the Einstein radius in the lens plane,

$$\xi_0 = \sqrt{\frac{4GM}{c^2}\frac{D_d D_{ds}}{D_s}}, \tag{10}$$

where G is the gravitational constant, M is the solar mass, c is the speed of light, D_d is the observer–lens distance, D_s is the observer–source distance, and D_{ds} is the lens–source distance. All coordinates are expressed in dimensionless form by scaling with ξ_0,

$$\mathbf{x} = \frac{\boldsymbol{\xi}}{\xi_0}, \qquad \mathbf{y} = \frac{\boldsymbol{\eta}}{\eta_0}. \tag{11}$$

Because each point on the source contributes light around the full circumference of the Einstein ring, the image observed at the detector is a convolution of the source brightness distribution with the SGL point spread function (PSF). For a monochromatic source, the SGL PSF is given by

$$\mathrm{PSF}(\rho) = \mu_0 \left[J_0^2\!\left(\frac{2\pi\rho}{\lambda}\sqrt{\frac{2GM_\odot}{c^2 z}}\right) + J_1^2\!\left(\frac{2\pi\rho}{\lambda}\sqrt{\frac{2GM_\odot}{c^2 z}}\right)\right], \tag{12}$$

where ρ is the radial coordinate in the image plane, λ is the wavelength, z is the heliocentric distance of the spacecraft, J_0 and J_1 are Bessel functions of the first kind, and μ_0 is the peak magnification factor.

The observed image is related to the true source image through convolution with the PSF. Recovering the source image therefore constitutes an inverse problem. In the Fourier domain, a regularized deconvolution may be written as

$$\hat{I}_{\mathrm{src}}(\mathbf{k}) = \frac{\hat{H}^*(\mathbf{k})}{|\hat{H}(\mathbf{k})|^2 + \gamma}\,\hat{I}_{\mathrm{obs}}(\mathbf{k}), \tag{13}$$

where $\hat{H}(\mathbf{k})$ is the Fourier transform of the PSF, γ is a regularization parameter, and $\hat{I}_{\mathrm{obs}}$ and $\hat{I}_{\mathrm{src}}$ are the Fourier transforms of the observed and reconstructed images, respectively. Regularization is required to suppress noise amplification in spatial frequency regions where the transfer function is small.

Successful image reconstruction depends critically on achieving sufficient SNR prior to deconvolution. In the background-dominated regime relevant to SGL observations, the SNR scales approximately as

$$\mathrm{SNR} \approx \frac{N_s}{\sqrt{N_b}}\sqrt{T}, \tag{14}$$

where N_s is the signal photon rate, N_b is the background photon rate dominated by residual solar corona light, and T is the integration time. This relationship highlights that image recovery is fundamentally limited by photon statistics rather than computational speed, necessitating long integration times to enable stable inversion.

Hardware

The Payload and OBC simulation was also verified through a hardware-in-the-loop demonstration. It is important to note that the flight mission would not directly capture a standard image of the target planet. In the real mission, the payload would collect light from the Einstein ring over time while the spacecraft moves through the SGL focal region, and the OBC would reconstruct the source planet from those ring brightness measurements. Since a true Solar Gravitational Lens cannot be reproduced in a laboratory environment, our demonstration uses a known planet image as the truth source. This image is captured by a camera or loaded from file, then processed into a synthetic Einstein ring. The reconstruction step then uses the ring-derived data, not the original image directly, to produce the final 2D image product. This lets us verify the part of the mission that can be tested on Earth: once ring measurements are available, the software can organize, reconstruct, store, and display the resulting image products.

The physical demonstration uses a Raspberry Pi 5 as the main OBC authority and an NVIDIA Jetson Orin Nano as the dedicated image reconstruction processor. The Raspberry Pi handles the command and data handling role. This includes scheduling, subsystem telemetry, mission event logging, output storage, file management, and dispatching processing jobs to the Jetson. The Jetson acts as the payload reconstruction co-processor. It receives the generated ring observation data, runs the staged reconstruction process, and returns image products back to the OBC-side storage. This division of work follows the same logic as the selected OBC architecture: one processor remains responsible for spacecraft control, data ownership, and autonomy, while a separate processor handles the computationally heavy image reconstruction. The same separation of responsibility is used in the project software, where the Pi is treated as the system authority and the Jetson is treated as the controlled accelerator node. [13]

The demonstration pipeline begins with a planet image, either from the camera or from a saved image file. The software preconditions the image by centering the planet, preserving the source geometry, and converting it into the square source canvas used by the ring-generation model. From there, the payload simulation generates an Einstein-ring observation and unwraps the ring into annular samples. The reconstruction software then builds the planet image progressively. A coarse image is produced first, followed by higher-resolution upscaled and refined products. This staged approach is useful for the actual mission because it allows low-resolution science products to be available earlier, while additional measurements and processing time are used to improve higher-resolution products.

The Jetson reconstruction node uses CUDA acceleration for the ring-to-image reconstruction pipeline, with CPU fallback available for validation, portability, and fault tolerance. In the demonstration, the software supports local processing, TCP-based Pi-to-Jetson processing, and backend selection between CPU and CUDA modes. This allows the same software pipeline to run on a development machine, on the Raspberry Pi alone, on the Jetson alone, or in the intended distributed Pi-to-Jetson configuration. The CUDA path is used to accelerate the computationally expensive reconstruction operations on the Jetson, while the CPU path provides a safe fallback if the accelerator is unavailable. This is important for a long-duration mission because science processing should degrade gracefully rather than fail completely if a processing node or accelerator becomes unavailable.

The hardware demonstration also includes a live telemetry and visualization dashboard. The dashboard displays subsystem states, power budget behavior, payload acquisition state, reconstruction progress, quality metrics, generated image products, and downlink queue behavior. This supports the mission concept because the spacecraft must operate autonomously over multi-day communication delays. The OBC must be able to decide when new science products are available, track reconstruction progress, preserve recent raw and processed data, and prepare products for downlink without requiring real-time ground intervention.

Although the demonstration uses a single Raspberry Pi 5 and a single Jetson Orin Nano, this should be interpreted as a proof-of-concept implementation rather than the final flight computer. The flight version would require radiation-tolerant or radiation-hardened electronics, watchdog recovery, error detection and correction, and redundant mass memory. The architecture is intentionally scalable. A future flight design could replace the single Jetson-class processor with a higher-memory processor, multiple reconstruction co-processors, or a clustered processing unit. This would allow the system to continue operating in a degraded mode if one processing node failed. Similarly, science products and ring measurements should be stored on an error-correcting and redundant mass-memory system, such as mirrored or erasure-coded solid-state storage, so that the loss of a single storage element would not end the science mission.

For this design phase, the hardware demonstration validates the software and data-handling concept rather than

prescribing the exact flight electronics. The Raspberry Pi represents the supervisory OBC behavior, while the Jetson represents a dedicated payload-processing unit. In the final spacecraft, these roles would be migrated to space-qualified hardware with appropriate radiation tolerance, redundant storage, and fault management. The test still provides useful verification because it demonstrates the complete data path from image acquisition, to ring generation, to CUDA-accelerated staged reconstruction, to telemetry display and product storage.

2. TT&C

A photon-counting optical link budget simulation was developed in MATLAB to evaluate the feasibility of the SGL downlink at a worst-case distance of 950 au. An initial attempt was made to model the link using STK; however, STK was unable to propagate the optical communication geometry at the unconventionally long range. As a result, a custom analytical model was necessary to directly capture the physical effects governing deep-space optical communications. The analysis is based on an optical formulation rather than a conventional RF approach. This is justified by the mission architecture, which uses a photon-counting receiver and pulse-position modulation (PPM), making detected photons the primary driver of link performance. The methodology evaluates:

1) Diffraction-limited beam divergence from the spacecraft transmit aperture,
2) Geometric spreading and interception of the beam at Earth,
3) Pointing-induced coupling loss,
4) Atmospheric and internal optical throughput losses,
5) Conversion of received optical power into detected photon rates,
6) Slot-level photon statistics for the selected PPM scheme,
7) Photon-efficiency link margin based on detected photons per information bit.

The optical carrier is characterized by the photon energy

$$E_\gamma = \frac{hc}{\lambda}, \tag{15}$$

which enables conversion between received power and photon count rate.

The diffraction-limited beam divergence is approximated by

$$\theta_{\text{div}} = 1.22\frac{\lambda}{D_{\text{tx}}}, \tag{16}$$

which sets the far-field beam spread. At a range R, the beam radius is

$$r_{\text{beam}} = \theta_{\text{div}} R, \tag{17}$$

and the fraction of power intercepted by the receive aperture is

$$\eta_{\text{geo}} = \frac{A_{\text{rx}}}{\pi r_{\text{beam}}^2}. \tag{18}$$

Residual pointing error is modeled as a Gaussian coupling loss

$$\eta_{\text{point}} = \exp\left[-2\left(\frac{\sigma_{\text{point}}}{\theta_{\text{div}}}\right)^2\right], \tag{19}$$

which reflects the sensitivity of narrow optical beams to microradian-level misalignment.

The received optical power is then given by

$$P_{\text{r}} = P_{\text{t}}\,\eta_{\text{tx}}\,\eta_{\text{geo}}\,\eta_{\text{point}}\,\eta_{\text{atm}}\,\eta_{\text{rx}}\,\eta_{\text{misc}}. \tag{20}$$

This power is converted into a detected photon rate using

$$N_{\text{sig}} = \frac{P_{\text{r}}}{E_\gamma}\,\eta_{\text{det}}, \tag{21}$$

which forms the basis of the link performance evaluation.

For the selected M-ary PPM scheme with code rate R_c, the slot duration is determined by

$$T_{\text{slot}} = \frac{1}{M R_{\text{sym}}}, \quad R_{\text{sym}} = \frac{R_b}{R_c \log_2 M}. \tag{22}$$

The detected signal photons per information bit are

$$n_{\text{sig,bit}} = \frac{N_{\text{sig}}}{R_b}, \tag{23}$$

and the optical link margin is defined as

$$M_{\text{link}} = 10 \log_{10} \left(\frac{n_{\text{sig,bit}}}{n_{\text{req,bit}}} \right), \tag{24}$$

where $n_{\text{req,bit}}$ is the required photons per information bit for reliable decoding.

This formulation is appropriate for the SGL mission because the link operates in a photon-limited regime at extreme distances, where received power is extremely low and traditional RF noise models are not representative of the dominant impairments. Using this methodology, the optical link budget theoretically proves such a system is capable of supporting reliable downlink communication at 950au, provided that pointing stability, atmospheric conditions, and background light are adequately controlled.

3. Flight Dynamics

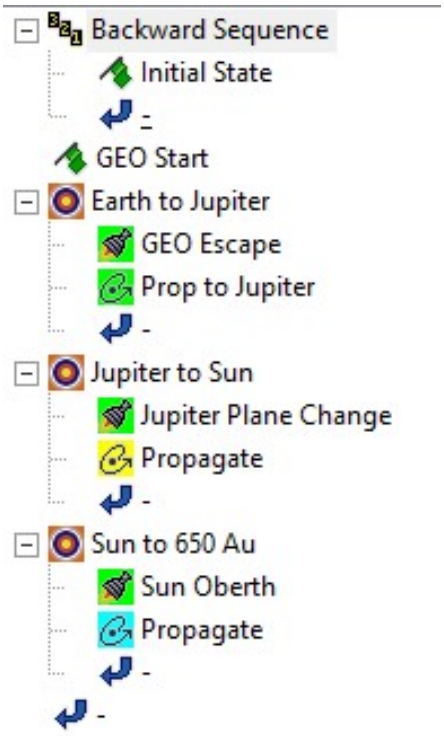

Fig. 16 Astrogator Mission Control Sequence (MCS) for the *Destiny* trajectory.

Ansys STK (Systems Tool Kit), developed by AGI, is premier software for modeling, simulating, and analyzing space, defense, and intelligence missions.

Its Astrogator module is a specialized, high-fidelity tool for spacecraft trajectory design, maneuver planning, and orbital determination, supporting missions from preliminary design to operations. Astrogator allows engineers to compute complex maneuvers, optimize fuel consumption, and simulate rendezvous and proximity operations. Key features used in our mission design include trajectory propagation with high-fidelity force models, maneuver targeting via differential correctors and Lambert solvers, and target sequences that use root-finding algorithms to satisfy mission constraints.

Mission Control Sequence Architecture. The trajectory was modeled in a Sun-centered STK scenario using a Backward Sequence in Astrogator's Mission Control Sequence (MCS), shown in Figure 16. The MCS is structured into three sequential legs, each containing an impulsive maneuver segment followed by a propagation segment:

Earth to Jupiter: A GEO Escape burn injects *Destiny* onto a heliocentric transfer ellipse, followed by a ~5-year propagation to Jupiter encounter. **Jupiter to Sun:** A Jupiter Plane Change maneuver at perijove (1.2 Jupiter radii) redirects the orbital plane toward the anti-Proxima Centauri b direction, followed by propagation on an inbound transfer to solar perihelion. **Sun to 650 au:** A Sun Oberth burn at perihelion (0.14 au) places the spacecraft on a hyperbolic escape trajectory, followed by propagation outward to the focal-line region.

All three legs used STK's built-in Lambert Solver profile to generate initial solutions for each transfer arc. The Lambert solver computes the conic trajectory connecting two position vectors over a specified time of flight, providing the departure and arrival velocity vectors from which the required ΔV at each node is derived. The resulting ΔV budget (Table 19) totals ~57.7 km/s for the three propulsive legs, representing an improvement over the prior RamDrag team's baseline of ~65 km/s.

Caveat: The Lambert solutions converge each leg independently and do not enforce a global constraint on the final asymptotic departure direction. As a result, the trajectory shown is not correctly aimed at the anti-Proxima Centauri b target; the architecture is sound, but the end-to-end optimization remains incomplete and would require a more experienced Astrogator user or SNOPT-level global optimizer to fully resolve.

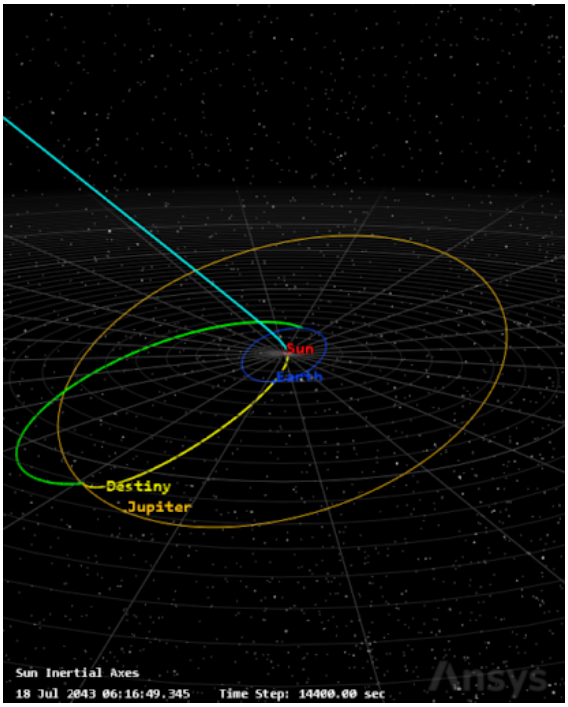

(a) Heliocentric view (Sun Inertial Axes). Green: Earth-to-Jupiter transfer; yellow: Jupiter's orbit; cyan: post-Solar Oberth hyperbolic escape toward 650 au.

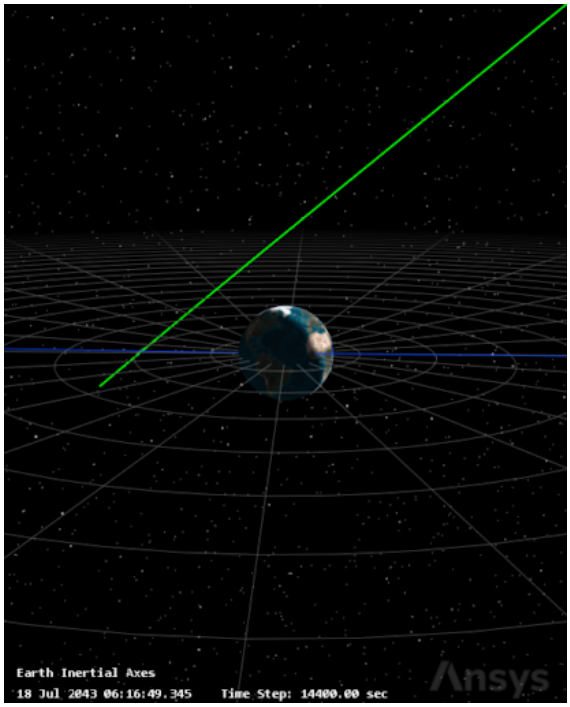

(b) Sun Inertial Axes view of the escape leg. The cyan trajectory departs the Sun toward the "Sun TargetPoint" at 650 au.

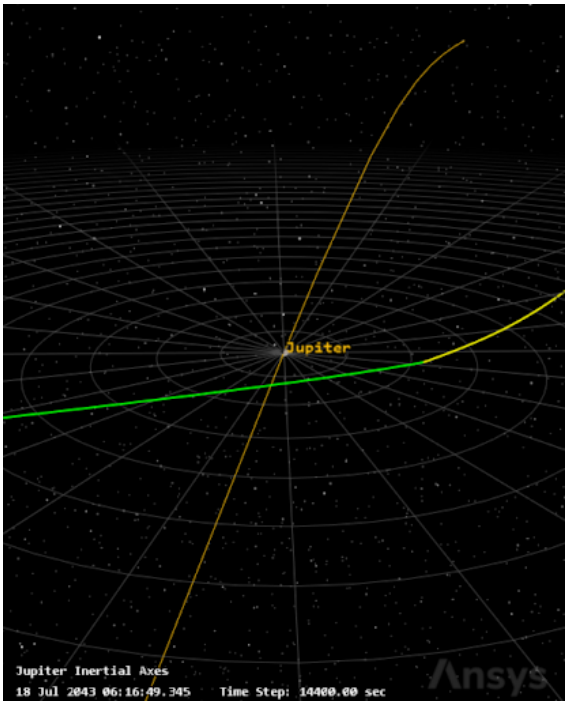

(c) Jupiter Inertial Axes view of the gravity-assist flyby. Green: inbound from Earth; yellow: departure toward solar perihelion; perijove at 1.2 Jupiter radii.

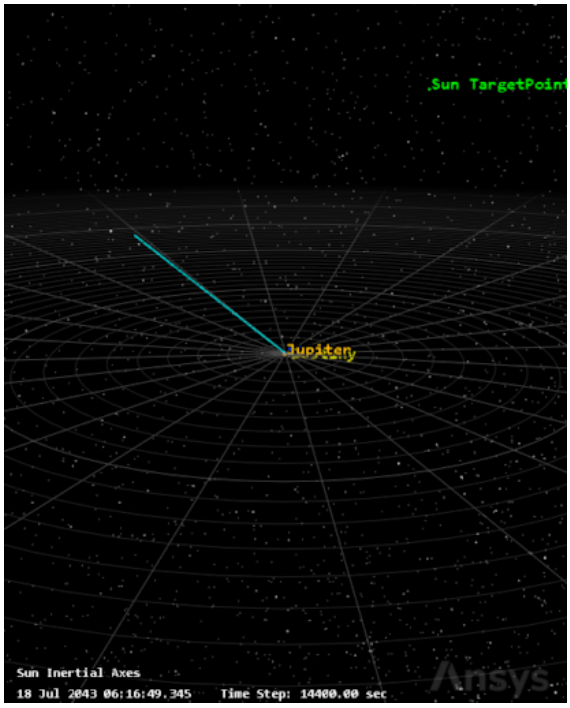

(d) Earth Inertial Axes view of GEO departure. The green line is the heliocentric transfer arc after the 12.5 km/s escape burn.

Fig. 17 STK Astrogator 3D trajectory visualizations of the *Destiny* mission, captured at epoch 18 Jul 2043, shown from four reference frames.

4. Propulsion

The simulation has multiple different situations, and each one will be explained here.

1. Pre-Solar Ion Propulsion

The way this simulation works is that it takes a certain exit velocity from Jupiter and simulates what would happen if you were to use the NEXT ion propulsion after the Jupiter Oberth. The mass values are not exact, but it does show the approximate effect this strategy would have.

The first step in the analysis is to calculate the mass of the solar panels, the mass of the ion fluid for a burn of 1.7 years, and add that to an approximate mass of 483 kg. Afterwards, some theoretical calculations are done to see the theoretical minimum perihelion velocity (do all the burn right after escaping Jupiter) and a theoretical maximum (all the burn right at perihelion). These values are achieved simply using conservation of energy:

$$\frac{V_1^2}{2} - \frac{\mu_s}{r_1} = \frac{V_2^2}{2} - \frac{\mu_s}{r_2} \tag{25}$$

To achieve the actual perihelion velocity we would achieve, a numerical integration is done using the forces from the Sun and the force from the thruster. The decrease in mass is also taken into to account. After all of the calculations, certain stats are given, such as the perihelion velocity, the time taken to do the maneuver, the mass ratio, and the ΔV gained from maneuver.

2. Post-Solar Ion Propulsion

First, all the different values from the NEXT Ion prop for different powers are put into different vectors for the code to sweep across. Next, the necessary weight of the generator needed to power the ion prop is calculated taking into the account the increase in mass from the half-life for 40 years. This mass is added to the dry mass of the craft.

Next, the mass for station keeping during imaging is calculated. This is included in most of the code later on, but the main equation used is:

$$R_{sk} = exp(\frac{V_t^2 * T_{sk}}{R_{sk} * u_{eq}}) \tag{26}$$

where V_t is the tangetial velocity for station keeping, T_{sk} is the amount of time in seconds of how long the craft will be doing the spiral, R_{sk} is the radius of the spiral, and u_{eq} is the equivalent velocity of the thruster.

Afterwards, a sweep is done for different burn times at different powers for the NEXT ion prop post solar Oberth to get the mass of the fuel. This is followed by calculating the mass ratio and then calculating the necessary effective V_∞ needed by the solar Oberth to reach 650 au in 40 years.

Lastly, the size of the solar sail is calculated. In order to this, some analysis of the sail is necessary. The force produced by an ideal sail is given by:

$$F_s = F_0 A cos^2(\theta)(1+\rho)(\frac{1au}{r})^2 \tag{27}$$

where F_0 is $4.54\frac{\mu N}{m^2}$ at 1 au, A is the area of the sail, θ is the angle between the normal vector of the sail with the position vector relative to the Sun, ρ is the reflectivity of the sail, and r is the distance from the center of the Sun. Because the force scales with the inverse square, we can actually convert this into an effective gravitational parameter:

$$\mu_{eff} = \mu_s - F_0\frac{A}{m}(1+\rho)(1au)^2 = \mu_s - k_s R \tag{28}$$

where μ_s is the gravitational parameter of the Sun and m is the mass of the spacecraft. This can be used in place of μ_s in our equations. Also note the simplification made here, where R is the sail area to spacecraft mass (including the sail) ratio. For this case, we calculate the necessary μ_{eff} to get the necessary effective V_∞. From there we get R. To get the sail size, we find the area to mass ratio of the craft before the sail by using:

$$R_0 = \frac{R}{1 - \rho_A R} \tag{29}$$

Where ρ_A is the areal density of the sail. By multiplying this with the appropriate weight, we get the necessary area of the sail to reach our goal within 40 years. The final mass is then calculated by multiplying the areal density with the sail area.

3. Standard/Aided

The last one has two cases merged together for ease of analysis. The first necessary thing is to determine the value of the first three ΔV's used in this mission. Note that for the value going away from Earth, there is an additional subtraction

of about 5.4 km/s to account for the additional energy that will be given by the carrier rocket. That value was calculated using the amount of energy the current Falcon Heavy gives for Mars-injection. Then, again using conservation of energy, determining how much ΔV in GEO would give you the equivalent energy.

After some setup, including the required V_p to reach the imaging plane within 40 years given by the STK, we can begin the calculating the aided solar burn case. To do so, we first sweep across a range of ΔV's for the chemical rocket. Now, in order to calculate the size of the sail, we need in some form the heliocentric energy required. Last time we used V_∞ because it was convenient, but in this case it is much more convenient to calculate the energy using V_p. After accounting for the burn we calculate that required energy, the change in energy necessary, and then finally using the following:

$$R = \frac{\Delta E r_p}{k_s} \tag{30}$$

we find the R of the sail. Now to make life easier, we can quickly find the mass ratio of the sail by using:

$$R_{sail} = \frac{1}{1 - \rho_A R} \tag{31}$$

and the mass ratio from the chemical propulsion with the rocket equation:

$$R_{chem} = exp(\frac{\Delta V_{chem}}{u_{eq}}) \tag{32}$$

Afterwards, the mass ratios from the spiral and hydrazine are determined using the rocket equation.

Lastly, the total masses of everything are determined using the structural coefficients of methalox and all the mass ratios. These values are plotted on a graph with the ΔV from the aided solar burn on the x-axis.

5. Mechanical

1. Matlab Stress Analysis

A first-order structural analysis of the selected truss configuration was carried out in MATLAB. The launch condition on the spacecraft yields a total axial compressive load of F_t = 1.4310^6 N, which is assumed to be shared equally among the four longerons, giving F_l = 3.5710^5 N per member. The cross-sectional area is approximately $0.0112m^2$, producing an axial stress of about 30 MPa, well below the yield strength of Ti-6Al-4V and giving a yield safety factor of roughly 9.3.

Buckling was evaluated using Euler's column formula for a pinned–pinned segment with effective length L_eff = 2 m, corresponding to the spacing between rings. The second moment of area of the outer beam cross-section about its strong axis was computed using an approximate solid rectangle minus inner cutout representation. With these properties and the Titanium alloy modulus E = 110.3 GPa, the critical buckling load for each 2 m segment was found to be approximately 8.410^5 N. Comparing this with the applied axial load per longeron gives a buckling safety factor of about 2.5.

The MATLAB script also performed parametric sweeps over wall thickness and section depth, generating plots of axial stress versus thickness and buckling safety factor versus thickness and depth. These parametric results confirm that increasing both the depth and wall thickness of the beams significantly improves buckling performance compared to earlier, shallower designs. These results are displayed in Figure 18

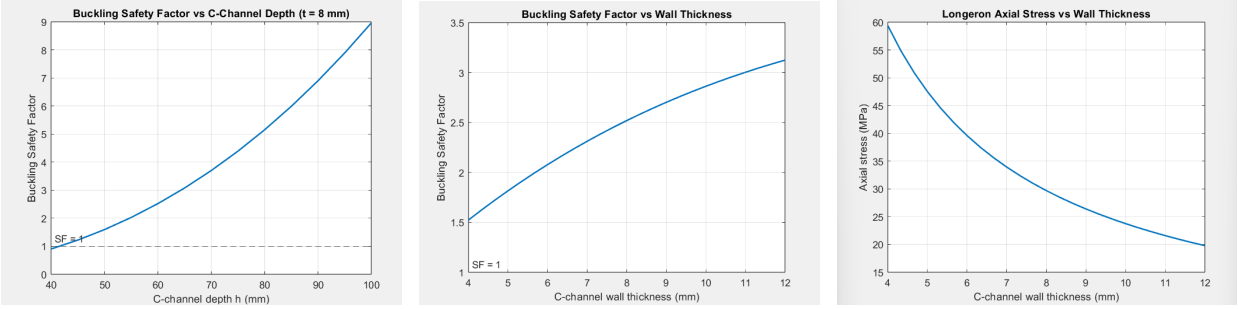

(a) Safety Factor vs Channel Depth **(b) Safety Factor vs Wall Thickness** **(c) Axial Stress vs Wall Thickness**

Fig. 18 Structural response metrics as a function of channel depth and wall thickness

2. FEMAP Approximation of force for frame

Additional analysis was performed in FEMAP to provide a more accurate simulation of the structural integrity of the frame. The Von Mises stress of our design is shown below in Figure 19.

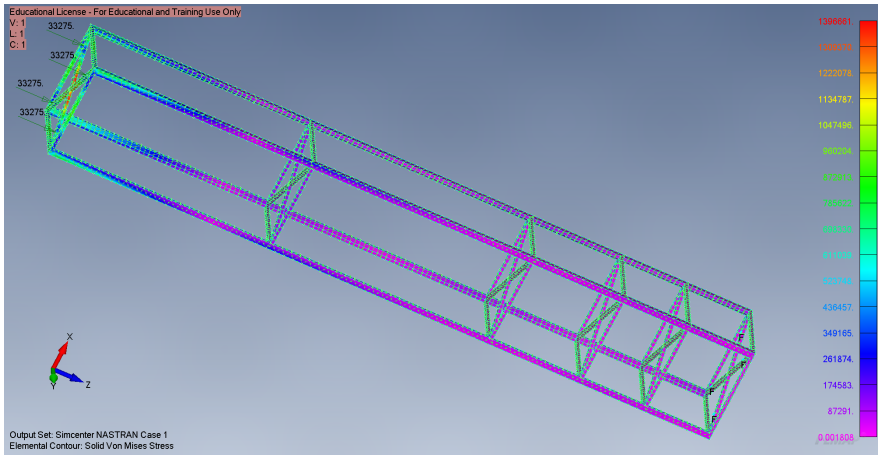

Fig. 19 FEMAP Plot of Von Mises Stress

In our FEMAP analysis of the maximum loading case, we stayed well underneath yield stress, reaching a Factor of Safety of 3.5, comfortably exceeding our target of 1.4. This excess will be necessary due to thermal concerns, especially in near-sun conditions. These FEMAP results are accepted with greater accuracy than the Matlab simulation, as it accounts for the full reaction of the structure and its complete geometry rather than simply examining the load bearing capabilities of the outer beams.

6. ADCS

The MATLAB-based closed-loop simulation was developed to evaluate the performance of the ADCS subsystem for the Solar Gravitational Lens (SGL) mission. The model made integrates star tracker measurements, gyro-based attitude propagation, onboard control logic, and reaction wheel actuation to replicate realistic spacecraft attitude behavior. The simulation begins with an initial attitude and rate error, which also demonstrates how the control system continuously corrects these deviations through feedback. The results show that the system is capable of reducing initial pointing error, damping angular rates, and maintaining a stable steady-state orientation under disturbance conditions. The pointing error, evaluated in arcseconds, converges toward the required 0.01 arcsecond accuracy, indicating that the ADCS architecture is capable of meeting mission-level precision requirements. Additionally, reaction wheel torque and speed remain within expected operational limits, as well as the system maintains stability in the presence of both disturbance torques and sensor noise. These results provide strong preliminary evidence that the closed-loop ADCS design is feasible for high-precision deep-space pointing.

To ensure that the simulation provides meaningful validation of the ADCS design, several system-level requirements must be satisfied. The simulation must accurately represent the full closed-loop control architecture, including sensor measurements, attitude estimation, control computation within the onboard computer, actuator response through reaction wheels, and the resulting spacecraft rotational dynamics. This complete representation ensures that all interactions between subsystems are captured and that feedback behavior is realistically modeled. The simulation must also evaluate high-precision pointing performance by computing the attitude error in arcseconds and directly comparing it to the mission requirement of 0.01 arcseconds.

Adding on, the simulation must incorporate disturbance modeling to represent environmental and internal torques that could affect spacecraft stability. Including both constant and time-varying disturbances ensures that the controller's robustness can be properly assessed. Sensor noise and estimation effects must also be included, particularly star tracker measurement uncertainty and gyro bias or drift, in order to reflect realistic sensing limitations and validate the effectiveness of the attitude determination process. Furthermore, actuator constraints must be enforced within the simulation by limiting reaction wheel torque and rotational speed, ensuring that control commands remain physically achievable and identifying any potential saturation behavior.

The dynamic response of the spacecraft must be modeled using rigid-body rotational equations and appropriate inertia properties so that the system accurately reflects how the spacecraft reacts to applied torques. Finally, the simulation must provide key performance outputs such as pointing error, angular rate response, and reaction wheel behavior over time. These outputs are essential for verifying system stability, evaluating control performance, and confirming that the ADCS meets mission requirements.

7. Electrical

The simulation for the electrical systems of the spacecraft is designed to verify the effectiveness of the radioisotope power systems by using the spacecraft requirements to calculate the energy balance equations, achieving a positive margin.

To demonstrate the spacecraft EPS satisfies the energy balance requirement over a representative operational cycle, we evaluate the inequality:

$$E_{in} - E_{out} \geq 0$$

To meet the system level requirements, the energy margin in the simulation must account for the energy output at the beginning of life, and scale with degradation at the end of life. This is due to the use of only RTG's as a power generation unit for the spacecraft, which naturally decays at a specific rate. The mechanical efficiency of the thermo-electric converters is also accounted for in this decay rate. It must also account for peak loads and peak load times, while having a comparison to nominal cruise load and load times during the 24 hour load schedule.

Though continuous power is supported throughout the 24-hour cycle, power contingency must exist as a fail-safe during peak loads and possible electrical downtime. With this in mind, the calculated requirements for the Nickel-Hydrogen batteries are also accounted for. The nominal cell number is found given the bus voltage requirements, and the mass is calculated based off of the stored energy totals. Depth of discharge is calculated to verify that the battery with stay within the required 40% during downlink.

8. Thermal

The thermal subsystem was analyzed using a first-order, two-node lumped-parameter transient model that represents the spacecraft bus and the critical On-Board Data Handling (OBDH) subsystem. This model was developed as an extension of the steady-state analysis and incorporates time-dependent behavior to evaluate the thermal response under bounding mission conditions. The governing energy balance for each node is expressed as:

$$mc_p \frac{dT}{dt} = \dot{Q}_{in} - \dot{Q}_{out} \tag{33}$$

where m is the effective mass of the node, c_p is the specific heat, and $\dot{Q}$ represents the net heat transfer rate. The model accounts for solar heating in the hot case, internal heat generation from subsystem power dissipation, and radiative heat rejection to deep space, conductive coupling between the bus and OBDH nodes, and thermostatically controlled heater input in the cold case. The equations were solved using an explicit forward Euler time-marching sequence. The two thermal environments in this model were simulated to assess survivability under extreme conditions. The hot case represents perihelion at 0.046 au, where the solar irradiance is maximized. The cold case represents deep-space conditions near 900 au, where external heating is negligible. Both of these environments are treated as fixed boundary conditions rather than a continuous trajectory simulation in order to provide a conservative evaluation of our thermal performance. The model assumes a lumped parameter representation with uniform temperature within each node, it includes heat transfer that is dominated by radiation and ignores convection, it assumes constant thermo-optical properties, and it models the effectiveness of the heat shield by using a lumped attenuation factor.

The simulation predicts a hot-case maximum temperature of 39.20 °C for the spacecraft bus and 47.39 °C for the OBDH subsystem. In the cold case, the minimum temperatures are −16.47 °C for the bus and −7.82 °C for the OBDH node. This is coupled with a peak heater demand of approximately 12 W. These results demonstrate the stability of the spacecraft thermal behavior from both of our nodes reaching steady-state equilibrium. The OBDH subsystem has an allowable operating range of −20 °C to 50 °C. The results from our simulation show that the hot-case OBDH temperature remains below the upper limit with a margin of 2.61 °C, while the cold-case temperature remains above the lower limit with a margin of 12.18 °C. This shows that the thermal subsystem satisfies the required temperature constraints for each of the bounding mission environments. Overall, the transient thermal simulation verifies that the selected hybrid thermal control architecture is capable of maintaining the spacecraft and its critical electronics within allowable temperature limits under both extreme hot and cold conditions.

B. Technical Standards and Professional Practice

The Solar Gravitational Lens mission follows standard aerospace engineering methods, using industry-regonized analysis tools to verify trajectory design, mechanical parameters, propulsion analysis, and ADCS dynamical verification. Trajectory design and gravity-assists were simulated in AGI STK Astrogator following accepted orbital mechanics principles. Numerical integration methods were used to calculate the optimal thrust parameters, while stress and Euler buckling theory was used to validate the structural mechanics through MATLAB. The electrical system also followed standard energy-balancing methods, accounting for RTG degradation and battery contingency. Thermal analysis used a two-node lumped parameter model to verify surviveability of the spacecraft in both hot and cold case environments.

XIV. Appendix

List of Figures

List of Tables

Code and Reproducibility

All code can be downloaded and used through the GitHub Repositiory at https://github.com/wyattowelch/AE460-Solar-Gravitational-Lens [14].

Payload & OBC

The image reconstruction itself is GPU-accelerated and staged, using a dedicated reconstruction processor to generate coarse products first and refine higher-resolution regions as additional measurements and compute time become available. This allows the OBC to return early image products for downlink while continuing to improve higher-resolution reconstructions over time.

Propulsion

Propulsion File List:

- FinalMassCalcs.m
- PostSolarIonProp.m
- PreSolarIon.m

How to Run:

FinalMassCalcs.m:

1) Download and open file,
2) Change any relevant information within the "Setup" section,
3) Run the code, and enjoy the results in the command window and graphs.

PostSolarIonProp.m:

1) Download and open file,
2) Change any relevant values within the "Ion Prop Calcs" section,
3) Run and enjoy the graphs.

PreSolarIon.m:

1) Download and open file,
2) Change any relevant information within the setup sections,
3) Run and enjoy the results in the command window.

Flight Dynamics

The simple calculator found in `SGL_Mission_FlightDynamics.m` returns theoretical guesses for our mission architecture. The program has sufficient comments to explain itself. The numbers it produces must be verified with robust, empirical solar system data such as those found in AGI Systems Tool Kit (STK). Please see section XIII.A.3 for more information about the STK simulation.

Note that `r_perihelion = 0.046 * au;` must be adjusted to match our decided $r_{perihelion}$ = 0.14 au.

Thermal

Thermal File List: The thermal simulation was implemented in MATLAB using a two-node lumped-parameter transient thermal model. The code used for this analysis is included in the project repository.

- final_thermal_simulation.m

How to Run:

To reproduce the thermal results presented in this report, follow these steps:

1) Open MATLAB and navigate to the directory containing the thermal simulation file.
2) Run the script
3) The script will automatically execute the transient simulation for both the hot and cold bounding cases.
4) Upon completion, the following outputs will be generated:
    - Command window summary of maximum and minimum temperatures
    - Temperature vs time plot (hot and cold cases)
    - Temperature vs heliocentric distance plot

TT&C

TT&C File List:

- optical_link_budget_spring_2026_final_report.m

How to Run:

1) Open MATLAB and open the TT&C simulation file.
    - No additional toolboxes are necessary
2) Run the script
3) Review results in the Command Window

Electrical

Electrical File List:

- ElecticalSim.m

How to Run:

1) Open MATLAB and open the Electrical simulation file.
    - No additional toolboxes are necessary
2) Input required power and variable adjustments
3) Run the script
4) Review results in the Command Window

ADCS

ADCS File List: The script created here implements a MATLAB-style attitude determination and control - simulation based on our teams PDR architecture: - 4 star trackers (Sodern SED16 model) - 4 reaction wheels in a pyramid configuration (Honeywell HR04 model) - OBC closes the loop using tracker/gyro inputs - mission mode here requires ultra-fine pointing

- Destiny_SGL_ADCS.m

1) Open MATLAB and open the ADCS Simulations file.
    - No additional toolboxes are necessary
2) Run the script
3) Review results in the Command Window

Mechanical

Mechanical File List:

- StructuralStressAnalysis.m

How to Run:

1) Open MATLAB and open the Structural Stress Analysis file.
    - No additional toolboxes are necessary
2) Run the script
3) Review results in the Command Window

Additional Analyses

Solar Sail Readiness Level

The solar sail has gone through many challenges and iterations. NASA pioneered early work, with some key missions ending in unfortunate failure. Relevant to this paper however is how developed the solar sails were. The first use of a sail was in 2010 with the IKAROS mission where the sail had areal density of 20 g/m^2 and area of 196 m^2, and since then the technology has improved rapidly.[15] The most developed solar sail to date comes 10 years later from an uncompleted NASA project in called "Solar Cruiser." The goal of the project is not relevant; however, during the development they created a quarter of the sail with an areal density of approximately 6 g/m^2, thickness of 2.5 microns, and total planned area of 1653 m^2. [16]. Although this seems far from the 1 g/m^2 necessary for the mission, this speedy progression within only the last 10 years yields great promise that within the 25 years given for the mission, a solar sail of that density can be developed. The main problem however is the size. Although it has been shown that structural a

sail of that size is within reach with current materials, [17] creating a solar sail that large is quite difficult in the gravity of Earth. During development and testing the sail will sag greatly. Additionally, finding a place to store and test the sail is also difficult. It is difficult to predict how far we will reach towards this, so this is why the sail is given a rating of 3: it seems like preliminary results have been created but there is still a lot of work to come.

References

[1] Turyshev, S. G., and Toth, V. T., "Navigating stellar wobbles for imaging with the solar gravitational lens," *Phys. Rev. D*, Vol. 105, No. 4, 2022, p. 044012. https://doi.org/10.1103/PhysRevD.105.044012, URL https://arxiv.org/abs/2112.03019.

[2] Turyshev, S. G., and Toth, V. T., "Image formation for extended sources with the solar gravitational lens," *Phys. Rev. D*, Vol. 102, 2020, p. 024038. https://doi.org/10.1103/PhysRevD.102.024038, URL https://arxiv.org/abs/2002.06492.

[3] Turyshev, S. G., Shao, M., Toth, V. T., Friedman, L. D., Alkalai, L., Mawet, D., Shen, J., Swain, M. R., Zhou, H., Helvajian, H., Heinsheimer, T., Janson, S., Leszczynski, Z., McVey, J., Garber, D., Davoyan, A., Redfield, S., and Males, J. R., "Direct Multipixel Imaging and Spectroscopy of an Exoplanet with a Solar Gravity Lens Mission," *arXiv preprint*, 2020. URL https://arxiv.org/abs/2002.11871.

[4] Turyshev, S. G., and Toth, V. T., "Spectrally resolved imaging with the solar gravitational lens," *Phys. Rev. D*, Vol. 106, No. 4, 2022, p. 044059. https://doi.org/10.1103/PhysRevD.106.044059, URL https://arxiv.org/abs/2206.03037.

[5] Bird, M. K., and Edenhofer, P., "Remote Sensing Observations of the Solar Corona," *Physics of the Inner Heliosphere I*, Physics and Chemistry in Space, Vol. 20, edited by R. Schwenn and E. Marsch, Springer-Verlag, 1990, pp. 13–97. https://doi.org/10.1007/978-3-642-75361-9_2, URL https://ui.adsabs.harvard.edu/abs/1990pihl.book...13B.

[6] Chasse, J., "Unveiling the Giants: Mid-Infrared Observations of the Solar System's Largest Planets," *Spectroscopy Supplement*, Vol. 39, No. s10, 2024, pp. 10–14. https://doi.org/10.56530/spectroscopy.wb6884v6, URL https://www.spectroscopyonline.com/view/unveiling-the-giants-mid-infrared-observations-of-the-solar-system-s-largest-planets.

[7] Bailey, V. P., Bendek, E., Monacelli, B., Baker, C., Bedrosian, G., Cady, E., Douglas, E. S., Groff, T., Hildebrandt, S. R., Kasdin, N. J., Krist, J., Macintosh, B., Mennesson, B., Morrissey, P., Poberezhskiy, I., Subedi, H. B., Rhodes, J., Roberge, A., Ygouf, M., Zellem, R. T., Zhao, F., and Zimmerman, N. T., "Nancy Grace Roman Space Telescope Coronagraph Instrument Overview and Status," *arXiv preprint*, 2023. URL https://arxiv.org/abs/2309.08672.

[8] NASA, "Dawn Mission," https://science.nasa.gov/mission/dawn/, 2024. Accessed: 2026-05-04.

[9] Busek, "BET-MAX Electrospray Thruster System," Tech. rep., Busek, 2021. URL https://static1.squarespace.com/static/60df2bfb6db9752ed1d79d44/t/61292b0fa097083a87c4ce1f/1630087953271/BETMAX_v1.0.pd.

[10] Patterson, M. J., and Benson, S. W., "NEXT Ion Propulsion System Development Status and Capabilities," Tech. Rep. NASA/TM-2008-214988, NASA Glenn Research Center, 2008. URL https://ntrs.nasa.gov/api/citations/20080012602/downloads/20080012602.pdf.

[11] Group, A. T., "SP0-S: 3U cPCI Radiation Tolerant PowerPC SBC," Datasheet 305-0027-01_E, Aitech Defense Systems, Inc., Nov. 2018. URL https://www.artisantg.com/info/Aitech_Defense_Systems_SP0_S_Datasheet_2020328133754.pdf, rev. 2.4.

[12] STAR-Dundee, "An Overview of the SpaceWire Standard," STAR-Dundee, ???? URL https://www.star-dundee.com/spacewire/getting-started/an-overview-of-the-spacewire-standard/.

[13] Team Destiny, "AE460 Solar Gravitational Lens Mission Repository," https://github.com/wyattowelch/AE460-Solar-Gravitational-Lens, 2026. Senior design simulation and hardware demonstration repository, San Diego State University. Accessed: 2026-05-15.

[14] Welch, W. O., "AE460-Solar-Gravitational-Lens: Simulation tools for SGL imaging and mission analysis," https://github.com/wyattowelch/AE460-Solar-Gravitational-Lens, 2024.

[15] Tsuda, Y., Mori, O., Funase, R., et al., "Achievement of IKAROS - Japanese Deep Space Solar Sail Demonstration Mission," *Acta Astronautica*, Vol. 82, 2013, pp. 183–188. https://doi.org/10.1016/j.actaastro.2012.03.032.

[16] NASA, "Solar Cruiser: Enabling New Vistas for Heliophysics Science," https://science.nasa.gov/heliophysics/programs/technology/solar-cruiser/, 2024.

[17] Zeiders, G. W., "Design Rules and Scaling for Solar Sails," Tech. rep., The Sirius Group, 2005. URL https://ntrs.nasa.gov/api/citations/20050209955/downloads/20050209955.pdf.

Acknowledgments

Nomenclature

A	=	Area used in thermal, sail, aperture, or detector-integration calculations [m^2]
A_{pix}	=	Area of one detector pixel [m^2]
A_{proj}	=	Projected area exposed to solar radiation [m^2]
A_{rx}	=	Ground receiver aperture area [m^2]
$ADCS$	=	Attitude Determination and Control System
AIV	=	Assembly, Integration, and Verification
APD	=	Avalanche photodiode
$APPLE$	=	Atomic Planar Power for Lightweight Exploration
au	=	Astronomical Unit
BoL	=	Beginning of Life
CAD	=	Computer-Aided Design
CCD	=	Charge-Coupled Device
$CCSDS$	=	Consultative Committee for Space Data Systems
$C\&DH$	=	Command and Data Handling
C_{Ah}	=	Required battery capacity [Ah]
c	=	Speed of light [m/s]
c_p	=	Specific heat capacity [J/(kg·K)]
$COTS$	=	Commercial Off-the-Shelf
CPU	=	Central Processing Unit
d	=	Annual RTG degradation fraction [-]; telescope aperture diameter where used in SNR reconstruction [m]
D	=	Component diameter, where used [m]; image-plane pixel spacing in SGL image reconstruction [m]
D_d	=	Observer-to-lens distance in the SGL model [m]
D_s	=	Observer-to-source distance in the SGL model [m]
D_{ds}	=	Lens-to-source distance in the SGL model [m]
D_{pix}	=	Image-plane pixel spacing for a reconstructed image pixel [m]
D_{rx}	=	Receive aperture diameter [m]
D_{tx}	=	Transmit aperture diameter [m]
$\frac{dT}{dt}$	=	Temperature rate of change [K/s]
ΔE	=	Required change in heliocentric specific energy [J/kg]
$\Delta\lambda$	=	Spectral bandwidth integrated in the SNR estimate [m]
Δt	=	Detector integration time used in the SNR estimate [s]
ΔV	=	Required maneuver velocity change [m/s or km/s]
$DIPA$	=	Disturbance Isolation and Pointing Assembly
DMS	=	Degrees-Minutes-Seconds coordinate format
DOD	=	Depth of Discharge
$DOD_{\max}$	=	Maximum allowable battery depth of discharge [-]
DSN	=	Deep Space Network
$DSOC$	=	Deep Space Optical Communications
DTE	=	Direct-to-Earth communications link
$EDAC$	=	Error Detection and Correction
EKF	=	Extended Kalman Filter
E_γ	=	Photon energy [J]
E_{in}	=	Energy supplied over an operating cycle [Wh]
E_{load}	=	Energy required by the contingency load [Wh]
E_{margin}	=	Remaining energy margin after loads are supplied [Wh]
E_{out}	=	Energy consumed by spacecraft loads over an operating cycle [Wh]
E_{req}	=	Required usable battery energy for contingency operation [Wh]
E_{stored}	=	Total stored battery energy [Wh]
E_{usable}	=	Usable battery energy at the allowed depth of discharge [Wh]

EoL = End of Life
EPS = Electrical Power System
$FDIR$ = Fault Detection, Isolation, and Recovery
FEC = Forward Error Correction
FDS = Flight Dynamics Subsystem
F_l = Axial launch load carried by one longeron [N]
F_s = Solar-sail force [N]
F_t = Total axial launch load [N]
F_0 = Solar radiation pressure force per unit area at 1 au [N/m^2]
FLT = Flight Laser Transceiver
G = Thermal conductance in the thermal model [W/K]; gravitational constant where used in SGL equations
GEO = Geostationary Earth Orbit
GNC = Guidance, Navigation, and Control
GPU = Graphics Processing Unit
$\hat{H}(\mathbf{k})$ = Fourier-domain point spread function transfer function
H = Component height, where used [m]
HMS = Hours-Minutes-Seconds coordinate format
I = Second moment of area for structural members [m^4]
$\hat{I}_{obs}$ = Fourier transform of the observed image
I_{sp} = Specific impulse [s]
$\hat{I}_{src}$ = Fourier transform of the reconstructed source image
IR = Infrared
J_0, J_1 = Bessel functions of the first kind
JPL = Jet Propulsion Laboratory
$JWST$ = James Webb Space Telescope
k_s = Solar-sail pressure constant used in the effective gravity model
L_{atm} = Atmospheric loss [dB]
L_{eff} = Effective column length for buckling analysis [m]
L_{point} = Pointing loss [dB]
LCH_4 = Liquid methane propellant
$LEOP$ = Launch and Early Operations
LOX = Liquid oxygen oxidizer
m = Mass or effective thermal-node mass [kg]
m_{batt} = Estimated battery mass [kg]
M = Solar mass in lensing equations; PPM order in link-budget equations
M_{link} = Optical link margin [dB]
MCS = Mission Control Sequence
$MHW\text{-}RTG$ = Multi-Hundred Watt Radioisotope Thermoelectric Generator
MLI = Multilayer Insulation
MOC = Mission Operations Center
$MOPA$ = Master-Oscillator Power-Amplifier
MR = Mission Requirement
$NASA$ = National Aeronautics and Space Administration
N = Number of reconstructed image pixels [-]
N_b = Background photon rate in the SNR estimate [s^{-1}]
N_{bkg} = Detected background photon rate [s^{-1}]
N_{cells} = Number of battery cells in series
N_s = Signal photon rate in the SNR estimate [s^{-1}]
N_{sig} = Detected signal photon rate [s^{-1}]
$NEXT$ = NASA Evolutionary Xenon Thruster
NiH_2 = Nickel-Hydrogen battery chemistry
$n_{req,bit}$ = Required detected photons per information bit
$n_{sig,bit}$ = Detected signal photons per information bit
$n_{sig,slot}$ = Detected signal photons per PPM slot

OBC = On-Board Computer
$OBDH$ = On-Board Data Handling subsystem
PCb = Proxima Centauri b
PCU = Power Control Unit
pc = Parsec
PD = Proportional-Derivative control
PDR = Preliminary Design Review
P_{in} = Electrical input power [W]
$P_{nominal}$ = Nominal spacecraft load power [W]
P_{out} = Electrical output or load power [W]
P_{peak} = Peak spacecraft load power [W]
P_r = Received optical power [W or dBW]
P_t = Transmitted optical power [W]
$P_{\mathrm{RTG},BoL}$ = RTG beginning-of-life power [W]
PPM = Pulse-Position Modulation
PSF = Point Spread Function
Pu-238 = Plutonium-238 radioisotope fuel
$\dot{Q}_{cond}$ = Conductive heat transfer rate between nodes [W]
$\dot{Q}_{heater}$ = Heater power input [W]
$\dot{Q}_{in}$ = Total heat input to a node [W]
$\dot{Q}_{out}$ = Total heat output from a node [W]
$\dot{Q}_{rad}$ = Radiative heat loss to space [W]
$\dot{Q}_{solar}$ = Absorbed solar heat input [W]
$Q_{\max}$ = Maximum heater power [W]
R = Solar-sail area-to-mass ratio, where used [m^2/kg]
R_0 = Area-to-mass ratio of the spacecraft before sail mass is included [m^2/kg]
$R_\oplus$ = Earth radius used as the source-planet radius scale in SGL image-plane mapping [m]
R_b = Information bit rate [bps]
R_c = Error-correction code rate [-]
R_{chem} = Chemical-propulsion mass ratio [-]
R_{sail} = Solar-sail mass ratio [-]
R_{sk} = Station-keeping or spiral-radius term, where used
R_{sym} = PPM symbol rate [symbols/s]
r = Heliocentric distance [au or m]
r_{beam} = Far-field optical beam radius [m]
r_p = Perihelion radius [au or m]
RF = Radio Frequency
RHU = Radioisotope Heater Unit
RPS = Radioisotope Power System
RTG = Radioisotope Thermoelectric Generator
$RTOS$ = Real-Time Operating System
$S(r)$ = Solar flux at heliocentric distance r [W/m^2]
S_0 = Solar flux at 1 au [W/m^2]
$SDSU$ = San Diego State University
SE = Battery specific energy [Wh/kg]
SGL = Solar Gravitational Lens
SKD = Skutterudite thermoelectric converter material
SNR = Signal-to-Noise Ratio
$\mathrm{SNR}(x_0, x_i, t, \lambda)$ = Local SNR density per unit detector area, wavelength, and time
SNR_C = Convoluted or pre-deconvolution SNR [-]
SNR_R = Resolved or reconstructed SNR after deconvolution [-]
$SNOPT$ = Sparse Nonlinear Optimizer
$SP0$-S = Aitech radiation-tolerant cPCI computer used as the central bus computer
STK = Systems Tool Kit

T = Temperature in thermal equations [K]; total observing or integration time where used in SNR equations [s]
T_{off} = Heater deactivation temperature threshold [K]
T_{on} = Heater activation temperature threshold [K]
T_{sk} = Station-keeping or imaging-spiral duration [s]
T_{slot} = PPM slot duration [s]
T_{space} = Deep-space background temperature [K]
TCS = Thermal Control Subsystem
TCM = Trajectory Correction Maneuver
TDC = Time-to-Digital Converter
TPS = Thermal Protection System
TRL = Technology Readiness Level
$TRIAD$ = Tri-Axial Attitude Determination method
$TT\&C$ = Telemetry, Tracking, and Control subsystem
t = Time or event duration [s or hr]
$t_{downlink}$ = Duration of a downlink segment [hr]
$t_{nominal}$ = Duration of nominal operation [hr]
t_{yr} = Mission elapsed time [yr]
u_{eq} = Equivalent exhaust velocity [m/s]
V_{bus} = Regulated spacecraft bus voltage [V]
V_{cell} = Nominal cell voltage [V]
V_p = Perihelion velocity [m/s]
V_{string} = Battery string voltage [V]
V_t = Tangential velocity for station keeping [m/s]
V_∞ = Hyperbolic excess velocity [m/s]
$YDFA$ = Ytterbium-Doped Fiber Amplifier
α = Surface absorptivity [-]
$\boldsymbol{\alpha}$ = Gravitational deflection angle in the lens equation [-]
γ = Deconvolution regularization parameter [-]
δ = Declination angle [DMS]
ϵ = Surface emissivity [-]
η = Efficiency factor, as defined locally [-]
η_{atm} = Atmospheric optical throughput [-]
η_{det} = Detector efficiency [-]
η_{geo} = Geometric beam-capture efficiency [-]
η_{misc} = Miscellaneous optical throughput [-]
η_{point} = Pointing coupling efficiency [-]
η_{rx} = Receiver optical efficiency [-]
η_{shield} = Heat-shield and geometry attenuation factor [-]
η_{tx} = Transmitter optical efficiency [-]
η_0 = Source-plane scaling length in the SGL model [m]
θ = Solar-sail angle relative to the Sun-line [rad]
θ_{div} = Optical beam divergence half-angle [rad]
λ = Optical wavelength, including mid-IR observing wavelength where used [m]
μ_0 = Peak SGL magnification factor [-]
μ_{eff} = Effective solar gravitational parameter with sail acceleration [m^3/s^2]
μ_s = Solar gravitational parameter [m^3/s^2]
ρ = Image-plane radial coordinate in SGL optics, or sail reflectivity where locally defined
ρ_A = Solar-sail areal density [kg/m^2]
σ = Stefan-Boltzmann constant [$W/(m^2K^4)$]
σ_{axial} = Axial stress in a structural member [Pa]
σ_{point} = RMS pointing error used in optical coupling loss [rad]
$\boldsymbol{\xi}$ = Dimensional lens-plane coordinate [m]
ξ_0 = Einstein-radius length scale in the lens plane [m]
$\boldsymbol{\eta}$ = Dimensional source-plane coordinate [m]

$\mathbf{x}$	=	Dimensionless image-plane coordinate [-]
x_0	=	Telescope position in the SGL image plane [m]
x_i	=	Detector focal-plane pixel position [m]
z	=	Heliocentric distance to the spacecraft or telescope along the SGL focal line [au or m]
z_0	=	Distance to the target exoplanet system [pc or m]
$\mathbf{y}$	=	Dimensionless source-plane coordinate [-]